

# BUMP ATTRACTORS AND WAVES IN NETWORKS OF LEAKY INTEGRATE-AND-FIRE NEURONS

DANIELE AVITABILE <sup>\*</sup>, JOSHUA L. DAVIS <sup>†</sup>, AND KYLE C. A. WEDGWOOD <sup>‡</sup>

**Abstract.** Bump attractors are wandering localised patterns observed in in vivo experiments of spatially-extended neurobiological networks. They are important for the brain’s navigational system and specific memory tasks. A bump attractor is characterised by a core in which neurons fire frequently, while those away from the core do not fire. These structures have been found in simulations of spiking neural networks, but we do not yet have a mathematical understanding of their existence because a rigorous analysis of the nonsmooth networks that support them is challenging. We uncover a relationship between bump attractors and travelling waves in a classical network of excitable, leaky integrate-and-fire neurons. This relationship bears strong similarities to the one between complex spatiotemporal patterns and waves at the onset of pipe turbulence. Waves in the spiking network are determined by a firing set, that is, the collection of times at which neurons reach a threshold and fire as the wave propagates. We define and study analytical properties of the *voltage mapping*, an operator transforming a solution’s firing set into its spatiotemporal profile. This operator allows us to construct localised travelling waves with an arbitrary number of spikes at the core, and to study their linear stability. A homogeneous “laminar” state exists in the network, and it is linearly stable for all values of the principal control parameter. Sufficiently wide disturbances to the homogeneous state elicit the bump attractor. We show that one can construct waves with a seemingly arbitrary number of spikes at the core; the higher the number of spikes, the slower the wave, and the more its profile resembles a stationary bump. As in the fluid-dynamical analogy, such waves coexist with the homogeneous state, and the solution branches to which they belong are disconnected from the laminar state; we provide evidence that the dynamics of the bump attractor displays echoes of unstable waves, which form its building blocks.

**1. Introduction.** Understanding how networks of coupled, excitable units generate collective patterns is a central question in the life sciences and, more generally, in applied mathematics. In particular, the study of network models is ingrained in neuroscience applications, as they provide a natural way to describe the interaction of neurons within a population, or of neural populations within the cortex. In the past decades, a large body of work in mathematical neuroscience has addressed the development and analysis of neurobiological networks, with the view of studying the origin of large-scale brain activity [36, 14, 22], and mapping single-cell and population parameters to experimental observations, including in vivo and in vitro cortical waves [73, 49, 45], electroencephalogram recordings [81], and patterns in the visual cortex [18].

This paper presents a novel mathematical characterisation of a prominent example of spatiotemporal pattern in neuroscience applications, and draws an analogy inspired by recent progress in the fluid-dynamics literature on transition to turbulence in a pipe [7]. We focus on the so-called *bump attractor*<sup>1</sup>, a localised pattern of neural activity observable in experiments and numerical simulations of spatially-extended, neurobiological networks [71, 92]. Bump attractors have been associated to *working memory*, the temporary storage of information in the brain, and experimental evidence

---

<sup>\*</sup>Department of Mathematics, Vrije Universiteit Amsterdam. Amsterdam Neuroscience, Systems & Network Neuroscience. MathNeuro Team, Inria Sophia Antipolis. [d.avitabile@vu.nl](mailto:d.avitabile@vu.nl), <https://www.danieleavitabile.com>.

<sup>†</sup>Defence Science and Technology Laboratory, Cyber and Information Systems Division.

<sup>‡</sup>Living Systems Institute, College of Engineering, Mathematics and Physical Sciences.

<sup>1</sup>In the neuroscience literature the term *bump attractor* refers sometimes to a network producing a localised pattern, as opposed to the pattern itself. Similarly, some authors use *ring attractor* for a network with ring topology, generating a localised activity bump. Here, we use these terms to refer to patterns, following the standard convention in the dynamical systems literature.

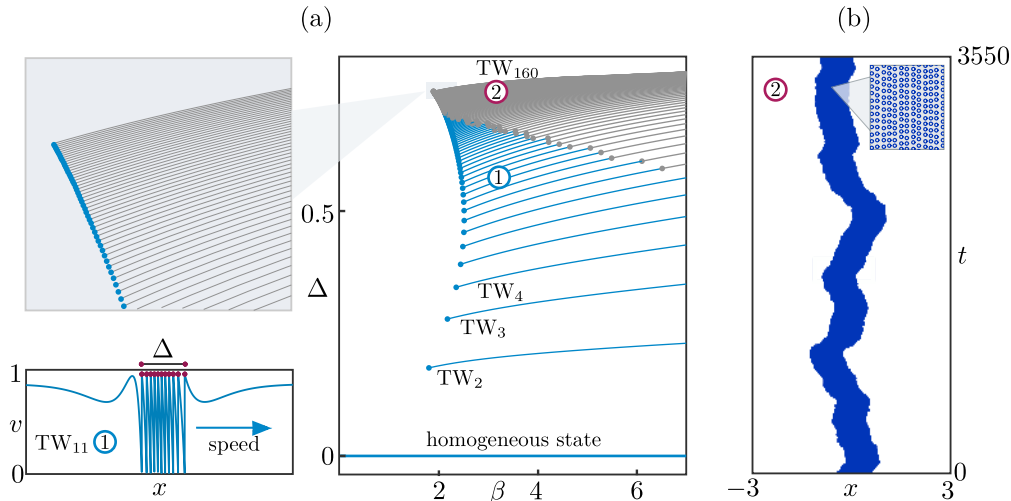


FIG. 1. (a) Bifurcation diagram of travelling waves in a continuous integrate-and-fire model. (b) Bump attractor in a discrete integrate-and-fire model with 5000 neurons (dots represent neuronal firing events, visible in the zoomed inset). Model descriptions and parameters will be given later in section 2, Table 1, and Figures 3 and 4). The bifurcation diagram in (a) shows selected branches of stable (blue) and unstable (grey) travelling waves, in the continuation parameter  $\beta$ , that is, the timescale at which neuron process incoming currents. Waves are measured using their width  $\Delta$  and are indexed by the number of advected spikes. The profile of  $TW_{11}$ , a representative wave with 11 spikes, is shown. A large number of waves ( $TW_2$ – $TW_{160}$  in the picture, but many more unstable branches are omitted) coexist with the trivial homogeneous state, which is the only steady state in the model, and which is stable for all values of  $\beta$ . Narrow waves are stable, with small basins of attraction. Sufficiently large, localised disturbances of the homogenous state lead to the formation of a bump with a characteristic width: the bump in (b) is marked as (2) in (a). The region in parameter space where bumps are observed is crowded with unstable travelling waves, with a large number of spikes, and a width comparable to the one of the bump. Branches of waves are detached from the homogeneous state; they originate at critical points called grazing points (blue dots in (a)); waves that are born stable become unstable at oscillatory bifurcations (grey dots in (a)).

supporting their existence has been found in the navigational systems of rats [54] and flies [53, 83], and in oculomotor responses of monkeys [90].

In a bump attractor, the neural activity is localised around a particular position in the network (see Figure 1(b)) which may encode, for instance, the animal’s head position. Bumps are elicited by transient localised stimuli, such as visual cues at specific locations, but are sustained autonomously by the network once the stimulus is removed (the network dynamics is *attracted* to the bump). These coherent structures display a characteristic wandering motion, and may exhibit discontinuous jumps if the impinging stimulus undergoes sudden spatial shifts [53].

**1.1. Model descriptions.** Mathematical neuroscience has a long-standing fascination with localised bumps of activity. Neural field models, which represent the cortex as a continuum, were introduced in the 1970s, and spatially-localised solutions to these models appeared already in seminal papers on the subject, by Wilson and Cowan [89], and by Amari [1]. Since then, many authors have studied localised solutions in neural fields, addressed the derivation of neural field equations from first principles, their relevance to a wide variety of neural phenomena, and their rigorous mathematical treatment. We refer the reader to [36, 14, 22] for exhaustive introduc-

tions on this topic.

Neural fields are integro-differential equations which model the cortex as an excitable, spatially-extended medium. Mathematical mechanisms for pattern formation in neural fields are similar to the ones found in other nonlinear media, such as reaction-diffusion systems, albeit their analysis requires some modifications because these models contain nonlocal operators. Stationary bumps form via instabilities of the homogeneous steady state, and their profile depends strongly on the coupling, which typically involves excitation on short spatial scales, and inhibition on longer scales [36, 14, 22]. Neural fields support travelling bump solutions, as well as wandering bumps. The latter are obtained in neural fields that incorporate stochastic terms deriving, for instance, from noisy currents [52, 62].

Neural fields are heuristic, coarse grained models, hence they bypass microscopic details that are important in bump attractors. For instance, the neural firing rate, which is an emergent neural property and an observable in the bump attractor experiments, is a prescribed feature in neural fields, hardwired in the model through an ad-hoc firing-rate function. On the other hand, numerical simulations of large networks of Hodgkin–Huxley-type neurons with realistic biological details can display emergent neural firing, but their mathematical treatment is challenging, and still under development [40, 4].

*Spiking neural networks* are intermediate, bottom-up models which couple neurons with idealised dynamics. The salient feature of spiking models is that the firing of a neuron is described as an event, and no attempt is made to model the temporal evolution of the membrane potential during and after the spike [51, 41, 14]. Spiking neural networks are specified by 3 main ingredients: (i) an ordinary differential equation (ODE) for the membrane potential of each neuron; (ii) rules to define the occurrence and effects of a spike; (iii) the network coupling.

Since the introduction of the first single-cell spiking model by Lapicque [59], the so-called *leaky integrate-and-fire model*, more realistic variants have been proposed, and spiking neural networks have become a widely adopted tool in theoretical neuroscience [82, 16, 41]. In specific spiking models, analytical progress has been made for single neurons and spatially-independent networks using coordinate transformations [35, 65], dimension reduction [61, 66], and probabilistic methods [27] (see also the reviews [76, 9]). Exact mean-field reductions, amenable to standard pattern-formation analysis, have been derived in selected spatially-extended networks [55, 37, 17, 78], but generally the study of bumps in spiking models has been possible only with numerical simulations [56, 19].

The present paper investigates localised patterns supported in discrete and continuous networks of nonlocally coupled leaky integrate-and-fire neurons. In direct numerical simulations, we use a well-known discrete model, proposed by Laing and Chow [56], whose details will be given later. For now it will suffice to consider a cursory formulation of the model, simulated in Figure 1(b). The network describes the idealised, dimensionless voltage dynamics of  $n$  all-to-all coupled neurons, evenly-spaced in a cortex with ring geometry,

$$(1.1) \quad \dot{v}_i = -v_i + I_i(t) + \sum_{j=1}^n S_{ij}(v_j, \beta), \quad i = 1, \dots, n.$$

The dynamics of the  $i$ th neuron’s membrane voltage is specified in terms of an Ohmic leakage current  $-v_i$ , an external current  $I_i(t)$ , and voltage-dependent currents, received from other neurons via synaptic connections; the latter currents, indicated by

$S_{ij}$ , have a characteristic time scale  $\beta$ , and are caused by  $v_j$  crossing a fixed threshold (when the  $j$ th neuron *fires*). After a firing event, marked with a dot in [Figure 1\(b\)](#) and its inset, the neuron’s voltage is instantly reset to a default value, from which it can evolve again, following an ODE of type [\(1.1\)](#). Discrete and continuous networks of this type are canonical models of neural activity, widely adopted in the mathematical neuroscience literature [[86, 85, 31, 32, 15, 56, 33, 68, 20, 67, 65, 42](#)]. It is now established that such networks support bump attractors and localised waves, but an explanation of the mathematical origins of the former is still lacking.

This paper presents a new approach to the problem, and uncovers a novel bifurcation structure for localised travelling waves of the network, shedding light onto the nature of the bump attractor. Our findings suggest an intriguing analogy between the bump attractor in the integrate-and-fire network and the phenomenon of transition to turbulence in a pipe. The analogy between the bifurcation scenarios of these two problems is notable, and we use it here to summarise our results, highlighting similarities between the respective bifurcation structures and dynamical regimes.

**1.2. Transition to turbulence in a pipe.** Stemming from the pioneering experiments of Reynolds [[72](#)], a large body of work in fluid dynamics has addressed how high-speed pipe flows transition from a laminar state, whose analytical expression is known in closed form, to complex spatio-temporal patterns, characteristic of the turbulent regime (see [[7](#)] for a recent review). In this context, the Navier-Stokes equations are studied as a deterministic dynamical system, subject to changes in Reynolds number, the principal control parameter. Experiments and computer simulations indicate that the laminar state is stable to infinitesimal perturbations (linearly stable) up to large values of the control parameter (up to at least Reynolds number  $10^7$  in numerical computations) [[77, 26, 64, 84, 63](#)]. However, when a disturbance is applied at sufficiently large Reynolds numbers, a transition to turbulence is observed, depending sensitively on the applied stimulus [[26, 47](#)]. Current opinions view the transition as being determined by *travelling wave solutions* to the Navier-Stokes equations [[79, 30, 38, 88, 69, 43](#)]. These invariant states, whose spatial profiles display hallmarks of the turbulent transition, coexist with the laminar state at intermediate Reynolds numbers, are linearly unstable, and provide an intricate blueprint for the dynamics, in that orbits may visit transiently these repelling solutions in phase space. Importantly, the waves lie on branches that are disconnected from the stable laminar state, and emerge at saddle-node bifurcations [[38, 88](#)]: this turbulence mechanism is therefore different from other paradigmatic routes to chaos, involving the destabilisation of the laminar state, and the progressive appearance of more complicated structures via a cascade of instabilities [[58, 48, 75](#)].

**1.3. Summary of results.** In a series of recent papers addressing turbulence from a dynamical-system viewpoint, Barkley proposed an analogy between pipe flows and excitable media, using the propagation of an electrical pulse along the axon of a neuron as a metaphor for localised turbulence puffs [[5, 6, 8, 7](#)]. The present paper offers a specular view, at a different scale: we are motivated by studying a canonical, complex neurobiological network of coupled excitable neurons, supporting localised spatio-temporal chaos, and we find a compelling similarity between the bifurcation structure of waves in this system, and the one of waves in the pipe turbulence.

With reference to [Figure 1](#), the principal control parameter of the problem is  $\beta$ , the timescale of synaptic currents: a low  $\beta$  gives small, persisting currents, while  $\beta \rightarrow \infty$  gives large instantaneous currents. A homogeneous steady state exists and is linearly stable for all values of  $\beta$  ( $\Delta = 0$  line in [Figure 1\(b\)](#)), but transient localised

stimuli trigger the bump attractor [56]. In the analogy, the homogeneous equilibrium plays the role of a “laminar state”. We stress that the homogeneous steady state is the only equilibrium of the model. Thus, the model can not support branches of stationary bump solutions. Instead, we demonstrate that travelling waves are key to understand the bump attractor.

We consider a spatially-continuous version of model (1.1), which is known to support waves advecting a low number of *localised spikes*, or having a non-localised profile [32, 12, 15, 33, 68]. The travelling waves of interest to us, however, have a localised profile, and advect a *large* number of spikes, such as the one presented in Figure 1(a). These structures are not accessible with the current techniques, hence we develop here analytical and numerical tools to construct them. We define particular type of solutions, which retain a fixed number of spikes in time; this class of solutions is sufficiently general to incorporate travelling waves with an arbitrary, finite, number of spikes, and small perturbations to them. We introduce the *voltage mapping*, a new operator which formalises an idea previously used in the literature for spiking [32, 12, 15, 33, 68, 3] and non-spiking networks [1, 36, 14, 22]. The voltage mapping is based on level sets describing firing events, and it allows efficient travelling wave constructions and stability computations.

Using the voltage mapping, we construct numerically waves with more than 200 concurrent spikes. These waves are spatially localised, and coexist with the trivial (laminar) state (see Figure 1(a)); most of the waves we computed are unstable, and the stable ones have a small basin of attraction. As in the turbulence analogy, the waves contain features of the bump attractor: they pack a seemingly arbitrary number of spikes within the width of a bump attractor, and they advect them at an arbitrarily slow speed, depending on  $\beta$ , and on the number of carried spikes. As in the fluid-dynamical analogy, waves are disconnected from the laminar state. Owing to the intrinsic non-smoothness of the network, the waves emerge primarily at grazing points (as opposed to the saddle-node bifurcations seen in the fluid-dynamical analogy, and also observed here in certain parameter regimes). In addition, we present numerical evidence that the transient dynamics to the bump attractor displays echoes of the unstable waves which, as in the fluid-dynamics analogy, form building blocks for the localised structure. Also, the characteristic wandering of the bump attractor, whose excursions become more prominent as  $\beta$  increases, is supported by this purely *deterministic* system, akin to the pseudo-stochastic behaviour observed in balanced neural networks [87, 60, 74].

The paper is structured as follows: in section 2 we introduce the discrete model, characterise it as a non-smooth threshold network, and present numerical simulations of bumps and waves; in section 3 we introduce the continuum model, the voltage mapping, and the construction of travelling waves; in section 4 we discuss travelling wave stability, we present numerical results in section 5, and we conclude in section 6.

**2. Coherent structures in the discrete model.** We begin by introducing the discrete model by Laing and Chow [56]. We characterise it as a piecewise-linear dynamical system, and we show numerical simulations of coherent structures. An important difference from the work by Laing and Chow is that we consider a *deterministic* model, which we call the Discrete Integrate-and-Fire Model (DIFM). We remark that the neurons considered here, taken in isolation, are in an *excitable regime*, that is, they exhibit an all-or-none response, based on the input they receive. This is considerably different from the so-called *oscillatory regime*, in which neurons, when decoupled from the network, display oscillations [86, 15, 65, 42].

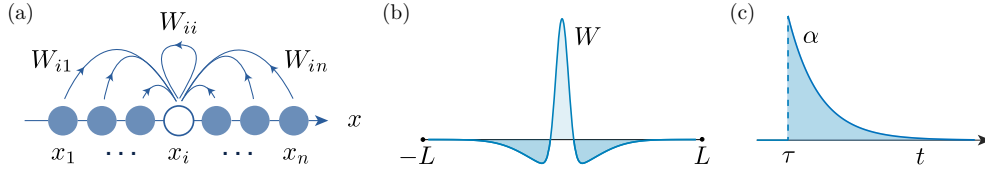


FIG. 2. (a): Schematic of the all-to-all coupled neurons with strengths  $W_{ik} = w(|x_i - x_k|)$ . In the model, we use a ring geometry, hence the left neighbour of  $x_1$  is identified with  $x_n$ , and the right neighbour of  $x_n$  with  $x_1$ . (b): The coupling (synaptic) function  $w(x)$  is chosen to be  $2L$ -periodic and positive (excitatory) on short spatial scales, and negative (inhibitory) on long spatial scales. (c) Time-dependent neuronal (post-synaptic) currents are modelled via the function  $\alpha$ , which is null before a neuron fires ( $t < \tau$ ), and exponentially decaying thereafter (see Equation (2.3)).

**2.1. Description of the DIFM.** The DIFM is a spatially-extended system of  $n$  identical *integrate-and-fire* neurons, posed on  $\mathbb{S} = \mathbb{R}/2L\mathbb{Z}$ , that is, a ring of period  $2L$ . Neurons are indexed using the set  $\mathbb{N}_n = \{1, \dots, n\}$  and occupy the discrete, evenly spaced nodes  $x_i = -L + 2iL/n \in \mathbb{S}$ , for  $i \in \mathbb{N}_n$ . Neurons are coupled via their synaptic connections, which are modelled by a continuous, bounded, even and exponentially decaying function  $w: \mathbb{S} \rightarrow \mathbb{R}$ : the strength of the connections from the  $k$ th to the  $i$ th neuron depends solely on the distance  $|x_i - x_k|$ , measured around the ring, hence we write it as  $W_{ik} = w(x_i - x_k)$ , for all  $i, k \in \mathbb{N}_n$  (see Figure 2). We note that  $w$  is  $2L$ -periodic by definition.

To the  $i$ th neuron is associated a real-valued time-dependent voltage function  $v_i(t)$ , and the coherent structures of interest are generated when voltages  $\{v_i\}$  attain a threshold value (when neurons *fire*). The DIFM is formally written as follows:

$$(2.1) \quad \dot{v}_i(t) = I_i(t) - v_i(t) + \frac{2L}{n} \sum_{k \in \mathbb{N}_n} \sum_{j \in \mathbb{N}} W_{ik} \alpha(t - \tau_k^j) - \sum_{j \in \mathbb{N}} \delta(t - \tau_i^j), \quad i \in \mathbb{N}_n,$$

$$(2.2) \quad v_i(0) = v_{0i}, \quad i \in \mathbb{N}_n.$$

At time  $\tau_i^j$ , when the voltage  $v_i$  reaches the value 1 from below for the  $j$ th time, a firing event occurs; a more precise definition of these *spiking times* will be given below. The formal evolution equation (2.1) expresses the modelling assumption that, when a neuron fires, its voltage is instantaneously reset to 0 (hence the Dirac delta), and a so-called *post-synaptic current* is received by all other neurons in the network, with intensity proportional to the strength of the synaptic connections. The time-evolution of this current is modelled via the *post-synaptic function*  $\alpha(t) = p(t)H(t)$ , expressed as the product of a continuous potential function  $p$  and the Heaviside function  $H$ , hence the post-synaptic current is zero before a spike.

In this paper, we present concrete calculations for

$$(2.3) \quad \alpha(t) = \beta \exp(-\beta t)H(t), \quad w(x) = a_1 \exp(-b_1|x|) - a_2 \exp(-b_2|x|),$$

with  $\beta, a_1, a_2, b_1, b_2 > 0$ , albeit the analytical and numerical framework presented below is valid for more generic choices, subject to general assumptions which will be made precise in subsection 3.2. The function  $\alpha$  models exponentially-decaying currents with rate  $-\beta$  and initial value  $\beta$ , hence the limit  $\beta \rightarrow \infty$  approximates instantaneous currents. Currents with an exponential rise and decay are also used in literature. The synaptic coupling function  $w$  is chosen so that connections are positive

(*excitatory*) on the lengthscale  $1/b_1$ , and negative (*inhibitory*) on the lengthscale  $1/b_2$  (see Figure 2).

In addition to the post-synaptic current, neurons are subject to an external stimulus  $I_i(t)$ . In certain time simulations, coherent structures will be elicited with the application of a transient, heterogeneous stimulus of the form

$$(2.4) \quad I_i(t) = I + d_1 H(\tau_{\text{ext}} - t) / \cosh(d_2 x_i), \quad i \in \mathbb{N}_n.$$

Our investigation, however, concerns asymptotic states of the autonomous homogeneous case  $I_i(t) \equiv I$ , hence one should assume  $d_1 = 0$ , unless stated otherwise. A description of model parameters and their nominal values can be found in Table 1.

**2.2. Event-driven DIFM.** Laing and Chow studied and simulated a stochastic version of the DIFM, using the Euler method and a first-order interpolation scheme to obtain the firing times [56]. We use here a different approach: in preparation for our analytical and numerical treatment of the problem, we write the formal model (2.1)–(2.2) as a system of  $2n$  piecewise-linear ODEs. To this end we introduce the synaptic input variables

$$(2.5) \quad s_i(t) = \frac{2L}{n} \sum_{k \in \mathbb{N}_n} \sum_{j \in \mathbb{N}} W_{ik} \alpha(t - \tau_k^j), \quad i \in \mathbb{N}_n$$

and combining (2.3) and (2.1) we obtain formally

$$\begin{aligned} \dot{v}_i(t) &= I_i(t) - v_i(t) + s_i(t) - \sum_{j \in \mathbb{N}} \delta(t - \tau_i^j) \\ \dot{s}_i(t) &= -\beta s_i(t) + \frac{2L\beta}{n} \sum_{k \in \mathbb{N}_n} \sum_{j \in \mathbb{N}} W_{ik} \delta(t - \tau_k^j) \end{aligned} \quad i \in \mathbb{N}_n.$$

One way to define the associated non-smooth dynamical system is to express the model as an impacting system, by partitioning the phase space  $\mathbb{R}^{2n}$  via a switching manifold, on which a reset map is prescribed (see [28] and references therein for a discussion on non-smooth and impacting systems). Here, we specify the dynamics so as to expose the firing times  $\{\tau_k^j\}$ , as opposed to the switching manifold: this is natural in the mathematical neuroscience context, and it prepares our analysis of the continuum model. Since  $\{\tau_k^j\}$  are the times at which orbits in  $\mathbb{R}^{2n}$  reach the switching manifold, a translation between the two formalisms is possible.

Following these considerations, we set  $\tau_i^0 = 0$  for all  $i \in \mathbb{N}_n$ , introduce the notation  $f(\cdot^\pm) = \lim_{\mu \rightarrow 0^+} f(\cdot \pm \mu)$ , and define firing times as follows<sup>2</sup>

$$(2.6) \quad \tau_i^j = \inf \{t \in \mathbb{R} : t > \tau_i^{j-1}, v_i(t^-) = 1, \dot{v}_i(t^-) > 0\}, \quad i \in \mathbb{N}_n, \quad j \in \mathbb{N}.$$

We arrange firing times in a monotonic increasing sequence  $\{\tau_{i_k}^{j_k}\}_{k=1}^q$  such that

$$(2.7) \quad (0, T] = \bigcup_{k \in \mathbb{N}_{q+1}} (\tau_{i_{k-1}}^{j_{k-1}}, \tau_{i_k}^{j_k}], \quad 0 = \tau_{i_0}^{j_0} < \tau_{i_1}^{j_1} \leq \dots \leq \tau_{i_q}^{j_q} < \tau_{i_{q+1}}^{j_{q+1}} = T,$$

for some time horizon  $T > 0$ , and obtain the desired set of  $2n$  piecewise-linear ODEs

$$(2.8) \quad \dot{v}_i = I_i - v_i + s_i, \quad \dot{s}_i = -\beta s_i \quad i \in \mathbb{N}_n, \quad t \in \bigcup_{k \in \mathbb{N}_{q+1}} (\tau_{i_{k-1}}^{j_{k-1}}, \tau_{i_k}^{j_k}],$$

<sup>2</sup>Note that  $\{\tau_i^0\}_i$  are not firing times, but auxiliary symbols for the definition of firing times (2.6). Indeed, since the sums in (2.1) run for  $j \in \mathbb{N}$ , the  $\{\tau_i^0\}_i$  are immaterial for the dynamics.

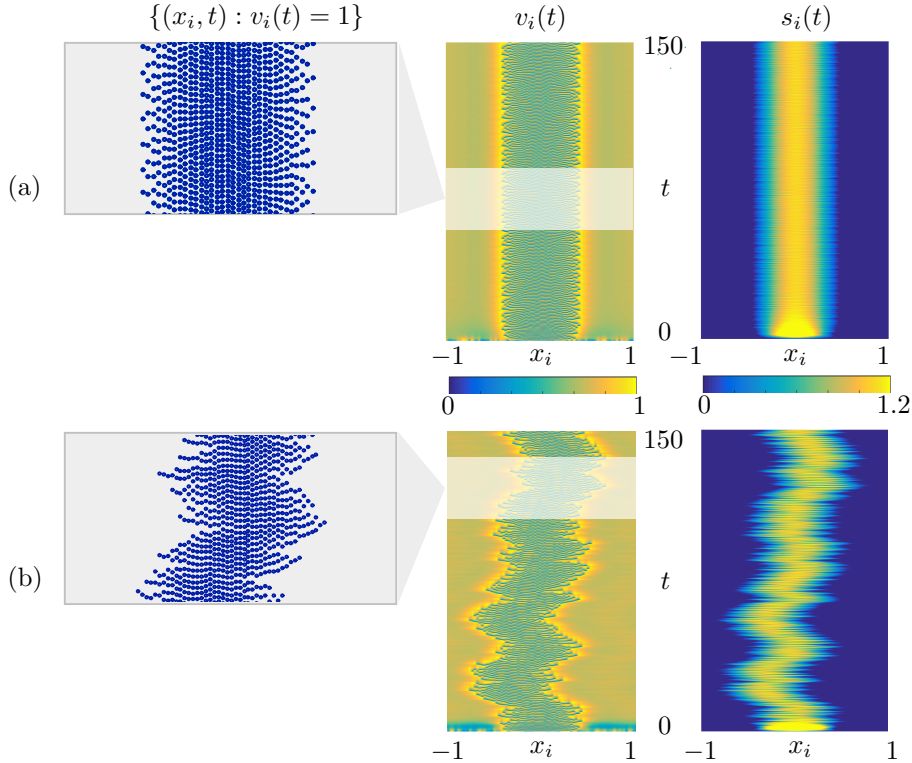


FIG. 3. Bump attractors obtained via direct numerical simulation of the DIFM (2.6)–(2.10) with external input (2.4) and connectivity function  $w$  as in (2.3). We visualise the network voltage (centre) and synaptic current (right) as functions of space and time and, in the inset (left), a raster plot of the firing events. Parameters as in Table 1 with  $n = 80$ ,  $d_1 = 2$   $d_2 = 10$ . The network’s synaptic time scale is  $\beta = 1$  (a) and  $\beta = 3.5$  (b), respectively. A localised coherent structure is visible in (a), which wanders when  $\beta$  is increased. We remark that the system under consideration is deterministic.

with initial and reset conditions

$$(2.9) \quad v_i(0) = v_{0i}, \quad s_i(0) = s_{0i}, \quad i \in \mathbb{N}_n,$$

$$(2.10) \quad v_{i_k}(\tau_{i_k}^{j_k+}) = 0, \quad s_l(\tau_{i_k}^{j_k+}) = s_l(\tau_{i_k}^{j_k-}) + \frac{2L\beta}{n} W_{li_k}, \quad l \in \mathbb{N}_n, \quad k \in \mathbb{N}_q,$$

respectively. Henceforth, we refer to the non-smooth dynamical system (2.6)–(2.10) with connectivity function  $w$  given by (2.3) and stimulus (2.4) as the *event-driven DIFM* or simply *DIFM*, that is, we view this model as a substitute for the formal system (2.1)–(2.2).

Even though the firing-time notation may seem cumbersome at first, the evolution of the DIFM is remarkably simple: Equation (2.8) states that between two consecutive firing times, neurons evolve independently, subject to a linear ODE; a solution in closed form can be written in terms of exponential functions, parametrised by the firing times. Constructing a solution amounts to determining firing times (impacts with the switching manifold), as is customary in piecewise-linear systems. This aspect will be a recurring theme in the sections analysing travelling waves in the continuum model.



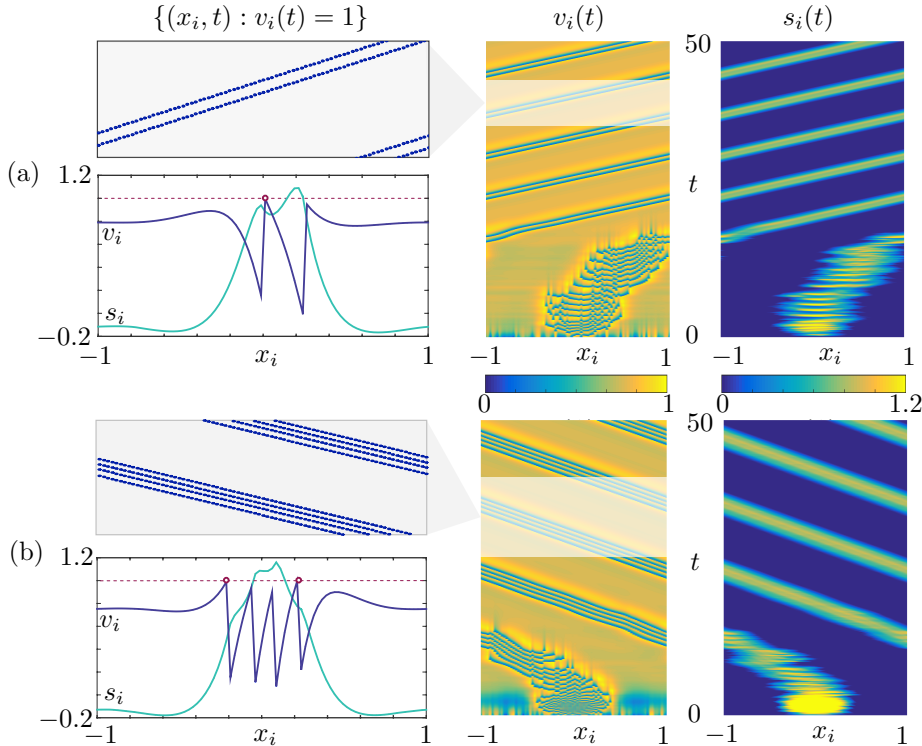


FIG. 4. *Stable coexistent waves obtained via direct numerical simulation of DIFM (2.6)–(2.10) with external input (2.4) and connectivity function  $w$  as in (2.3). Parameters as in Table 1 with  $n = 80$ ,  $\beta = 4.5$  for both (a) and (b), but different initial stimuli: (a)  $d_1 = 0.4$ ,  $d_2 = 12$ , (b)  $d_1 = 2$ ,  $d_2 = 10$ . Depending on the transient stimulus the model displays: (a) a wave propagating with positive speed, in which pairs of neurons fire asynchronously, but at short times from each other; (b) a similar structure involving a quartet of neurons. Coexisting structures with variable numbers of firing neurons have also been found (not shown). The spatial profiles indicate that neurons reach threshold (dashed red line) one at a time within a pair (a) or two at a time within a quartet (b).*

In simulations of the DIFM, we time step Equation (2.8) rather than using its analytic solution. We use an explicit adaptive 4-5th order Runge-Kutta pair with continuous output, and detect events (compute firing times) by root-finding [29, 80]. The simulation stops at each firing event and is restarted after the reset conditions (2.10) are applied. Simulating the event-driven DIFM instead of (2.1) allows us to compute firing times accurately, and to evolve the system without storing in memory or truncating the synaptic input sums in (2.1).

**2.3. Coherent structures in the DIFM.** The DIFM supports standing and travelling localised structures, as in the stochastic setting [56]. Bumps form robustly when we prescribe homogeneous initial conditions<sup>3</sup> with a short transient stimulus (Equation (2.4) with  $\tau_{\text{ext}} = 2$ ). Since  $I_i(t) \equiv I$  for all  $t > \tau_{\text{ext}}$ , the structures observed over long-time intervals are solutions to a homogeneous, non-autonomous problem.

As seen in Figure 3, the bump wanders when  $\beta$  is increased. In passing, we note

<sup>3</sup>Typically we set  $v_{0i} = u \in (0, 1)$ ,  $s_{0i} = 0$ , for  $i \in \mathbb{N}_n$ , but the coherent structures discussed in the paper can also be found with random, independent and identically distributed initial voltages, for instance  $v_{0i} \sim \mathcal{U}([0, 1])$ , where  $\mathcal{U}$  is the uniform distribution.

that this phenomenon is not due to stochastic effects, as studied in other contexts [52, 50, 3], because the DIFM is deterministic. For sufficiently large  $\beta$ , the system exhibits stable travelling structures: in Figure 4 we show two coexisting waves, found for  $\beta = 4.5$  upon varying slightly the width  $d_1$  and intensity  $d_2$  of the transient stimulus. In each case we plot the voltage and synaptic profiles, and associated raster plots. We notice different firing patterns in the waves, involving 2 and 4 firings, respectively: the wave with 2 firings travels faster, and its voltage and synaptic profiles are narrower. We found coexisting waves with a greater number of firings and progressively lower speed, whose existence and bifurcation structure will be at the core of the following sections.

**2.4. Remarks about coherent structures in the DIFM.** The patterns presented so far are found in the DIFM with a finite number of neurons ( $n = 80$ ). At first sight, the raster plots of the waves seem to indicate that neurons fire simultaneously in pairs (Figure 4(a)) or quartets (Figure 4(b)) as the structure travels across the network. A closer inspection of the instantaneous profiles  $v_i(t)$  reveal that this is not the case, as the threshold (red dashed line) is attained by a single neuron in Figure 4(a), and by two neurons in Figure 4(b): neurons in a raster pair fire alternately over a short time interval, whereas a quartet displays a more complex firing pattern.

Hence, for finite  $n$ , the propagating structures displayed in Figure 4 are not strictly travelling waves, in the sense that the profile is not stationary in the comoving frame; their dynamics is that of saltatory waves [23, 91, 3]. The saltatory nature of the waves, however, is an effect of the network size: as we increase  $n$ , the amplitude of temporal oscillations in the comoving frame scales as  $O(n^{-1})$ , and the spatio-temporal profile converges to one of a travelling wave as  $n \rightarrow \infty$ .

In addition, the structure in Figure 3(a) is not a bump, in the sense that it is not a spatially heterogeneous steady state of the DIFM, because the pattern is sustained by firing events (and the presence of firing events means the voltage changes in time). Indeed, the only equilibrium supported by the DIFM is the homogeneous state  $v_i(t) \equiv I$ ,  $s_i(t) \equiv 0$ ,  $i \in \mathbb{N}_n$ , which is linearly stable for all values of  $\beta$ , as can be deduced by inspecting system (2.8).

By constructing travelling waves and investigating their stability in a continuum version of the DIFM, we shall see that the structure in Figure 3(a) (and its wandering) can be interpreted as deterministic chaotic behaviour.

**3. Travelling waves in the continuum model.** As stated in section 2, the profiles  $\{v_i(t)\}_i$  and  $\{s_i(t)\}_i$  in Figure 4 behave like travelling wave solutions as  $n \rightarrow \infty$ . Motivated by this observation, we study travelling waves in a continuum, translation-invariant version of the DIFM: we set  $d_1 = 0$  in the stimulus (2.4), consider a continuum spatial domain, and pose the model on  $\mathbb{R}$  as opposed to  $\mathbb{S}$ , obtaining

$$(3.1) \quad \begin{aligned} \partial_t v(x, t) = & -v(x, t) + I + \sum_{j \in \mathbb{N}} \int_{-\infty}^{\infty} w(x - y) \alpha(t - \tau_j(y)) dy \\ & - \sum_{j \in \mathbb{N}} \delta(t - \tau_j(x)), \quad (x, t) \in \mathbb{R} \times \mathbb{R}. \end{aligned}$$

The formal evolution equation presented above, which we henceforth call the *continuous integrate-and-fire model* (CIFM), has been proposed and studied by several authors in the mathematical neuroscience literature [32, 44, 10, 12, 68, 67]. In the CIFM, firing-time functions  $\tau_j(x)$  indicate that the neural patch at position  $x$  fires

for the  $j$ th time, and replace the discrete model's firing times  $\tau_k^j$ .<sup>4</sup> A graph of the firing functions replaces the raster plot in the discrete model, so that a travelling wave in the CIFM corresponding to the  $n \rightarrow \infty$  limit of the structure in Figure 4(a), for instance, will involve 2 linear firing functions  $\tau_1, \tau_2$ , with  $\tau_1(x) < \tau_2(x)$  for all  $x \in \mathbb{R}$ .

The existence of travelling waves solutions in (3.1) with a single spike has been studied by Ermentrout [32] who presented various scalings of the wavespeed as a function of control parameters. A general formalism for the construction and linear stability analysis of *wavetrains* (spatially-periodic travelling solutions) was introduced and analysed by Bressloff [12], who derived results in terms of Fourier series expansions. The construction of travelling waves with multiple spikes was later studied by Oğan and coworkers [67], albeit stability for these states was not presented and computations were limited to a few spikes, for purely excitatory connectivity kernels. The common thread in the past literature on this topic is the idea that travelling wave construction and stability analysis rely entirely on knowledge of the firing function  $\tau_j$  (as in the DIFM, with firing times). A similar approach has been used effectively in Wilson-Cowan-Amari neural field equations, where it is often called *interfacial dynamics* (see [1] for the first study of this type, [21] for a recent review, and [24, 39], amongst others, for examples of spatio-temporal patterns analysis).

Here we present a new treatment of travelling wave solutions that draws from this idea; we introduce an operator, that we call the *voltage mapping*, with the following aims: (i) Expressing a mapping between firing functions and solution profiles, with the view of replacing the formal evolution equation (3.1) for travelling waves with  $m$  spikes (where  $m$  is arbitrary). (ii) Finding conditions for the linear stability of these waves. (iii) Using root-finding algorithms to compute travelling waves and study their linear stability. We will relate to existing literature in our discussion.

**3.1. Notation.** Before analysing solutions to the CIFM, we discuss the notation used in this section. We use  $\|\cdot\|_\infty$  to denote the  $\infty$ -norm on  $\mathbb{C}^m$ . We denote by  $C(X, Y)$  the set of continuous functions from  $X$  to  $Y$ , and use  $C(X)$  when  $Y = \mathbb{R}$ . We denote by  $B(X)$  ( $BC(X)$ ) the set of real-valued bounded (real-valued bounded, continuous) functions defined on  $X$ . Further, for a positive number  $\eta$ , we shall use the following exponentially weighted Banach spaces:

$$L_\eta^1(\mathbb{R}) = \left\{ u: \mathbb{R} \rightarrow \mathbb{R}: \|u\|_{L_\eta^1} = \int_{\mathbb{R}} e^{\eta x} |u(x)| dx < \infty \right\},$$

$$C_\eta(\mathbb{R}, \mathbb{C}^m) = \left\{ u \in C(\mathbb{R}, \mathbb{C}^m): \|u\|_{C_{m,\eta}} = \sup_{x \in \mathbb{R}} e^{-\eta|x|} |u(x)|_\infty < \infty \right\}.$$

**3.2. Characterisation of solutions to the CIFM via the voltage mapping.** We begin by discussing in what sense a voltage function  $v$  satisfies the CIFM formal evolution equation (3.1). While we eschew the definition of the CIFM as a dynamical system on a Banach space (a characterisation that is currently unavailable in the literature), we note that progress can be made for voltage profiles with a constant and finite number of spikes for  $t \in \mathbb{R}$ . This class of solutions is sufficiently large to treat travelling waves, and small perturbations to them.

We make a few assumptions on the network coupling, and we restrict the type of firing functions and solutions of interest, as follows:

---

<sup>4</sup>The index  $j$  is used as a superscript in the firing times, but for notational convenience we use it as a subscript in the firing functions, so that  $\tau_j(x_k) \approx \tau_k^j$ .

*Hypothesis 3.1* (Coupling functions). The connectivity kernel  $w$  is an even function in  $C(\mathbb{R}) \cap L^1_\eta(\mathbb{R})$ , for some  $\eta > 0$ . The post-synaptic function  $\alpha: \mathbb{R} \rightarrow \mathbb{R}_{\geq 0}$  can be written as  $\alpha(t) = p(t)H(t)$ , where  $H$  is the Heaviside function, and  $p: \mathbb{R}_{\geq 0} \rightarrow \mathbb{R}$  is a bounded and everywhere differentiable Lipschitz function, hence  $p, p' \in B(\mathbb{R})$ .

**DEFINITION 3.2** (*m-spike CIFM solution*). Let  $m \in \mathbb{N}$  and  $I \in \mathbb{R}$ . A function  $v_m: \mathbb{R}^2 \rightarrow \mathbb{R}$  is an *m-spike CIFM solution* if there exists  $\tau = (\tau_1, \dots, \tau_m) \in C(\mathbb{R}, \mathbb{R}^m)$  such that  $\tau_1 < \dots < \tau_m$  on  $\mathbb{R}$  and

$$(3.2) \quad v_m(x, t) = I + \sum_{j \in \mathbb{N}_m} \int_{-\infty}^t \int_{-\infty}^{\infty} \exp(z - t) w(x - y) \alpha(z - \tau_j(y)) dy dz \\ - \sum_{j \in \mathbb{N}_m} \exp(\tau_j(x) - t) H(t - \tau_j(x)), \quad (x, t) \in \mathbb{R}^2$$

$$(3.3) \quad v_m(x, t) = 1, \quad (x, t) \in \mathbb{F}_\tau,$$

$$(3.4) \quad v_m(x, t) < 1, \quad (x, t) \in \mathbb{R}^2 \setminus \mathbb{F}_\tau,$$

where

$$\mathbb{F}_\tau = \bigcup_{j \in \mathbb{N}_m} \{(x, t) \in \mathbb{R}^2 : t = \tau_j(x)\}.$$

We call  $\tau$  and  $\mathbb{F}_\tau$  the *firing functions* and the *firing set* of  $v_m$ , respectively.

The definition above specifies how we interpret solutions to (3.1), and is composed of three ingredients: (i) Equation (3.2), which derives from integrating (3.1) on  $(-\infty, t)$ , and expresses a mapping between the set of  $m$  firing functions  $\tau$  and the voltage profile; (ii) System (3.3), which couples the firing functions by imposing the threshold crossings; (iii) A further condition on  $v_m$ , ensuring that the solution has exactly  $m$  spikes, attained at the firing set; this is necessary because, as we shall see below, it is possible to find a set of  $m$  functions  $\tau$  satisfying Equations (3.2)–(3.3), but exhibiting a number of threshold crossings greater than  $m$ .

We now aim to characterise  $m$ -spike CIFM solutions by means of a *voltage mapping*, which can be conveniently linearised around a firing set, and is a key tool to construct waves and analyse their stability. Inspecting (3.2) we note that the voltage profile features two contributions, one from the (synaptic) coupling functions  $w$  and  $\alpha$ , and one from reset conditions. This observation leads to the following definitions:

**DEFINITION 3.3** (Synaptic, Reset, and Voltage mappings). Let  $u: \mathbb{R} \rightarrow \mathbb{R}$ . We define the *synaptic operator*,  $S$ , and the *reset operator*,  $R$ , by

$$(3.5) \quad (Su)(x, t) = \int_{-\infty}^t \int_{-\infty}^{\infty} \exp(z - t) w(x - y) \alpha(z - u(y)) dy dz, \quad (x, t) \in \mathbb{R}^2,$$

$$(3.6) \quad (Ru)(x, t) = -\exp(u(x) - t) H(t - u(x)), \quad (x, t) \in \mathbb{R}^2.$$

Further, let  $m \in \mathbb{N}$ ,  $I \in \mathbb{R}$  and  $\tau \in C(\mathbb{R}, \mathbb{R}^m)$ . The *m-spike voltage mapping*,  $V_m$ , is the operator defined as

$$(3.7) \quad V_m \tau = I + \sum_{j \in \mathbb{N}_m} (S\tau_j + R\tau_j).$$

These operators map univariate functions, such as a firing function, to bivariate functions, such as the spatio-temporal voltage profile. Under Hypothesis 3.1 it holds  $S: C(\mathbb{R}) \rightarrow BC(\mathbb{R}^2)$ ,  $R: C(\mathbb{R}) \rightarrow B(\mathbb{R}^2)$ , hence  $V_m: C(\mathbb{R}) \rightarrow BC(\mathbb{R}^2)$  (see A.1).

By construction, the voltage operator characterises  $m$ -spike CIFM solutions, as the following proposition shows.

**PROPOSITION 3.4.** *Let  $m \in \mathbb{N}$ ,  $I \in \mathbb{R}$ . An  $m$ -spike CIFM solution exists if, and only if, there exists  $\tau \in C(\mathbb{R}, \mathbb{R}^m)$  such that*

$$(3.8) \quad V_m \tau = 1, \quad \text{in } \mathbb{F}_\tau,$$

$$(3.9) \quad V_m \tau < 1, \quad \text{in } \mathbb{R}^2 \setminus \mathbb{F}_\tau$$

*Proof.* The statement follows by setting  $v_m(x, t) = (V_m \tau)(x, t)$  and applying the definition of the voltage mapping, [Equation \(3.7\)](#).  $\square$

[Proposition 3.4](#) implies that the voltage of an  $m$ -spike solution can be computed for any  $(x, t) \in \mathbb{R}^2$  once the firing functions  $\tau$  are known. The spatio-temporal profile of an  $m$ -spike solution is determined entirely by its firing functions. This aspect, which underlies the formal evolution equation [\(3.1\)](#) and the literature which analyses it, is a key part of what follows and, as we shall see below, it also suggests a natural way to compute travelling waves, and determine their linear stability. A first step in this direction is the definition of travelling waves via the voltage mapping.

**3.3. Travelling waves with  $m$ -spikes ( $TW_m$ ).** Following [Proposition 3.4](#), we can capture travelling waves with  $m$  spikes ( $TW_m$ ) using the voltage mapping, and a set of parallel firing functions. Henceforth, we will assume without loss of generality that the propagating speed of the wave is positive: for any wave with  $c > 0$ , there exists a wave with speed  $-c$ , and the wave profiles related by the transformation  $x \rightarrow -x$ .

**DEFINITION 3.5 ( $TW_m$ ).** *Let  $m \in \mathbb{N}$ ,  $c > 0$ , and let  $T \in \mathbb{R}^m$  with  $T_1 < \dots < T_m$ . A travelling wave with  $m$  spikes ( $TW_m$ ), speed  $c$ , and coarse variables  $(c, T)$  is an  $m$ -spike CIFM solution with firing functions  $\{\tau_j(x) = x/c + T_j\}_{j \in \mathbb{N}_m}$ .*

To each travelling wave solution is associated a travelling wave profile which is advected with propagation speed  $c$ . From [Proposition 3.4](#) we expect this profile to be determined entirely by the firing functions, as confirmed in the following result.

**PROPOSITION 3.6 ( $TW_m$  profile).** *A  $TW_m$  with speed  $c$  satisfies  $(V_m \tau)(x, t) = \nu_m(ct - x; c, T)$ , and its  $(c, T)$ -dependent travelling wave profile  $\nu_m$  is given by*

$$(3.10) \quad \begin{aligned} \nu_m(\xi; c, T) = & I - \sum_{j \in \mathbb{N}_m} \exp\left(-\frac{\xi - cT_j}{c}\right) H\left(\frac{\xi - cT_j}{c}\right) \\ & + \frac{1}{c} \sum_{j \in \mathbb{N}_m} \int_{-\infty}^{\xi} \exp\left(\frac{z - \xi}{c}\right) \int_0^{\infty} w(y - z + cT_j) p(y/c) dy dz. \end{aligned}$$

*Proof.* See [Appendix C](#).  $\square$

[Proposition 3.6](#) shows that the travelling wave profile is completely determined by the vector  $(c, T) \in \mathbb{R}_{>0} \times \mathbb{R}^m$ , that is,  $(c, T)$  is a vector of coarse variables for the travelling wave. In the discrete model we introduced an auxiliary spatially-extended variable for the model, the synaptic input  $\{s_i(t)\}_i$  defined in [\(2.5\)](#). In the continuum model, the corresponding variable is the function  $s_m(x, t) = \sum_{j \in \mathbb{N}_m} (S\tau_j)(x, t)$ , which in a  $TW_m$  satisfies  $s_m(x, t) = \sigma_m(ct - x; c, T)$ , with

$$(3.11) \quad \sigma_m(\xi; c, T) = \frac{1}{c} \sum_{j=1}^m \int_0^{\infty} w(y - \xi + cT_j) p(y/c) dy.$$

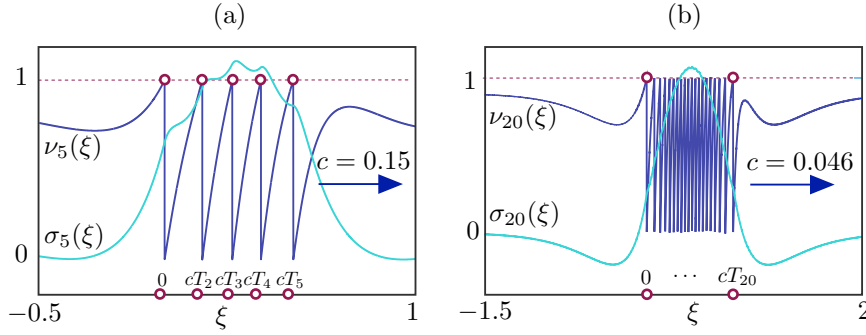


FIG. 5. Wave profiles for (a)  $TW_5$  and (b)  $TW_{20}$  obtained by solving [Problem 3.7](#) for  $m = 5$  and  $m = 20$ , respectively, and then substituting  $(c, T_1, \dots, T_m)$  into the expression for voltage profile [\(3.10\)](#) and synaptic profile [\(3.11\)](#). The profile  $\nu$  is computable at any  $\xi \in \mathbb{R}$ , here we plot it using an arbitrary grid in the intervals (a)  $[-0.5, 1]$  and (b)  $[-1.5, 2]$ . Parameters as in [Table 1](#) with (a)  $\beta = 4.5$  and (b)  $\beta = 7.7$ .

**3.4. Travelling wave construction.** [Proposition 3.6](#) suggests a simple way to compute a  $TW_m$ , by determining its  $m + 1$  coarse variables  $(c, T)$ , as a solution to the following coarse problem:

*Problem 3.7* (Computation of  $TW_m$ ). Find  $(c, T) \in \mathbb{R}_{>0} \times \mathbb{R}^m$  such that  $T_1 < \dots < T_m$  and

$$(3.12) \quad T_1 = 0,$$

$$(3.13) \quad \nu_m(cT_i^-; c, T) = 1, \quad \text{for } i \in \mathbb{N}_m,$$

$$(3.14) \quad \nu_m(\xi; c, T) < 1, \quad \text{on } \mathbb{R} \setminus \cup_{j \in \mathbb{N}_m} \{cT_j^-\}.$$

[Equation \(3.13\)](#) of the coarse problem imposes that the travelling wave profile crosses the threshold 1 when  $\xi \rightarrow cT_j^-$ , which is a necessary and sufficient condition to ensure  $\nu_m = 1$  in  $\mathbb{F}_\tau$  (see [Corollary B.1](#)). As expected, if  $\nu_m$  is a travelling wave profile, then so is  $\nu_m(\xi + \xi_0)$  for any  $\xi_0 \in \mathbb{R}$ ; [Equation \(3.12\)](#) fixes the phase of the travelling wave, by imposing that the profile crosses threshold as  $\xi \rightarrow 0^-$ .

If  $m = 1$ , [Equations \(3.12\)–\(3.13\)](#) of the coarse problem reduce to a compatibility condition for the speed  $c$ ,

$$c \int_{-\infty}^0 \int_0^{\infty} \exp(s) w(c(y-s)) p(y) dy ds = I - 1,$$

which implicitly defines an existence curve for  $TW_1$  in the  $(c, I)$ -plane. This result is in agreement with what was found in [\[67, 32\]](#). Existence curves in other parameters are also possible, and are at the core of the numerical bifurcation analysis presented in detail in the sections below.

For  $m > 1$ , the coarse problem must be solved numerically. A simple solution strategy is to find a candidate solution using Newton's method for the system of  $m + 1$  transcendental equations [\(3.12\)–\(3.13\)](#), with  $\nu_m$  given by [Proposition 3.6](#), and with initial guesses estimated from direct simulation of the discrete model with large  $n$ , or from a previously computed coarse vector. The candidate solution can then be evaluated at arbitrary  $\xi \in \mathbb{R}$ , hence it is accepted if [\(3.13\)](#) holds on a spatial grid covering  $[-L, L] \subset \mathbb{R}$ , with  $L \gg 1$ . In passing, we note that this procedure is considerably cheaper than a standard travelling wave computation for PDEs, which requires

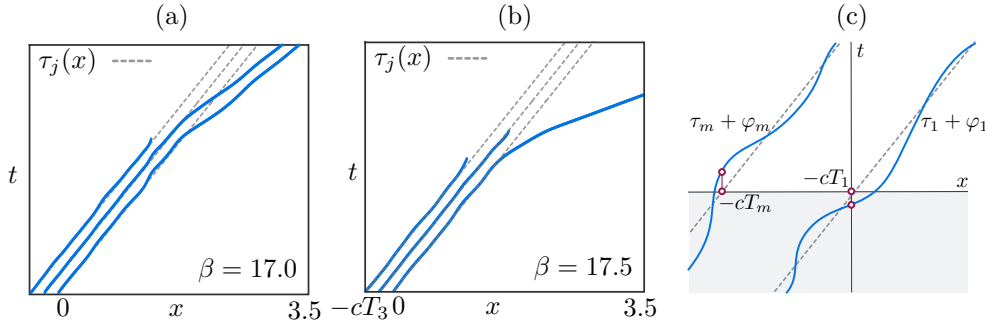


FIG. 6. (a)-(b): Examples illustrating the destabilisation of a  $TW_3$  solution. A time simulation of the DIFM is initialised using wave profiles obtained solving [Problem 3.7](#) for  $m = 3$  at (a)  $\beta = 17$  and (b)  $\beta = 17.5$ . Parameters as in [Table 1](#), domain half-width  $L = 4$  and network size  $n = 1000$ . The firing functions  $\{\tau_j\}$  are plotted for reference. Oscillatory perturbations to the firing functions do not decrease with time, hence the wave is unstable. The dynamics leads to stable (a)  $TW_2$  and (b)  $TW_1$  solutions. (c): Perturbations  $\tau + \varphi$  to the firing functions  $\tau$  of a  $TW_m$ . At  $t = 0$  each firing function  $\tau_i$  is perturbed by an amount  $\varphi_i(-cT_i)$ . A  $TW_m$  is linearly stable if  $\varphi_i(-cT_i)$  being small implies that  $\varphi_i(x)$  stays small for all  $x \in (-cT_i, \infty)$  and  $i \in \mathbb{N}_m$  (see [Definition D.3](#)).

the solution of a boundary value problem, and hence a discretisation of differential operators on  $\mathbb{R}$ . Depending on the particular choice of  $\alpha$  and  $w$ , the profile  $\nu_m$  is either written in closed form, as is the case for the choices [\(2.3\)](#), or approximated using standard quadrature rules.

A concrete calculation is presented in [Figure 5](#), where we show travelling wave profiles and speeds of a  $TW_5$  and a  $TW_{20}$ . In passing, we note that the synaptic profile of a  $TW_m$  at a given time is similar to a bump, but displays modulations at the core (visible in [Figure 5](#)), as predicted by the Heaviside switches in [\(3.11\)](#). Travelling waves with a large number of spikes, such as these ones, have not been accessible to date.

*Remark 3.8.* [Figure 5](#) shows that profiles with  $\nu_m(cT_j^-) = 1$  propagate with *positive* speed, and this does not contradict the numerical simulations in [Figure 4](#), where solutions profiles with  $\nu_m(x, \tau_j(x)^-) = 1$  propagate with *negative* speed. This is a consequence of choosing  $\xi = ct - x$  (as in [\[67\]](#)), hence initial conditions for the time simulations are obtained by reflecting  $\nu_m$  about the  $y$  axis, since  $\nu_m(x, 0) = \nu_m(-x)$ .

**4. Wave Stability.** The time simulations in [section 2](#) demonstrate that, for sufficiently large values of  $\beta$ , travelling waves with a variable number of spikes coexist and are stable. It is natural to ask whether these waves destabilise as  $\beta$ , or any other control parameter of the model, is varied. An example of a prototypical wave instability is presented in [Figure 6](#) for  $TW_3$ : a travelling wave is computed solving [Problem 3.7](#), and this solution is used as initial condition for a DIFM simulation with  $n = 1000$  neurons. For sufficiently large  $\beta$ , the wave is unstable, as exemplified by the raster plots in [Figure 6\(a\)–\(b\)](#), in that the firing functions never return to the ones of a  $TW_3$ .

[Figure 6](#) shows that the firing set of the solution is composed of 3 disjoint curves, initially close to the ones of a  $TW_3$ , from which they depart progressively. Ultimately, some firing functions terminate, and the dynamics displays an attracting  $TW_2$  or  $TW_1$ . Capturing the transitions from a  $TW_m$  to a travelling wave with fewer spikes is a nontrivial task. Studying the *nonlinear stability* is not possible with the current

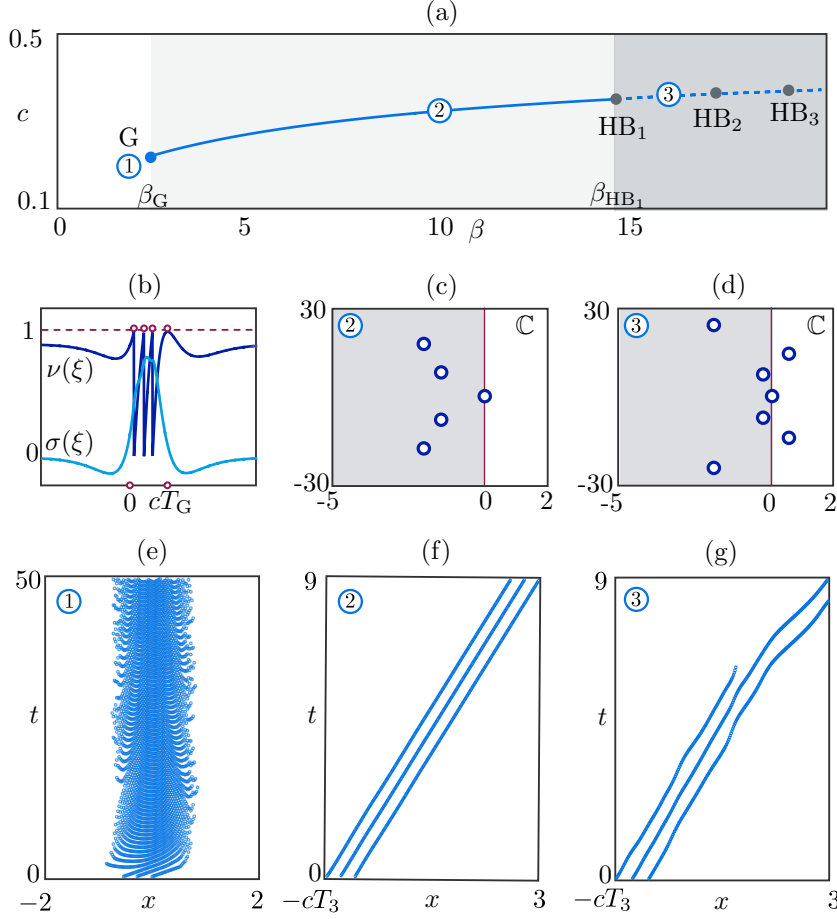


FIG. 7. (a) Branch of  $TW_3$  solutions in the parameter  $\beta$ , using  $c$  as solution measure. The branch originates at a grazing point  $G$ , illustrated by the profile in (b). As  $\beta$  increases, three pairs of complex conjugate roots of  $E$  (see Equation (D.7)) cross the imaginary axis at the oscillatory (Hopf) bifurcation points  $HB_1$ ,  $HB_2$ ,  $HB_3$ . Panels (c) and (d) show selected roots of  $E$ , before and after  $HB_1$ , at  $\beta = 10$  and  $16$ , respectively. (e)–(g) Raster plots for time simulations of the DIFM with  $n = 500$  and domain half-width  $L = 3$ , initialised from solutions to Problem 3.7 at  $\beta = 2.17$ ,  $10$ , and  $16$ , respectively. The simulations show the dynamics of the model for  $\beta < \beta_G$  (where a  $TW_3$  does not exist in the continuum limit), for  $\beta \in (\beta_G, \beta_{HB_1})$  (where  $TW_3$  is stable according to the analysis in (c)), and for  $\beta > \beta_{HB_1}$  (where  $TW_3$  is unstable to oscillatory perturbations, as predicted in (d)). Parameters as in Table 1, with  $d_1 = 0$ .

definition of CIFM solutions, which require a constant number of spikes. The voltage mapping, however, opens up the possibility of studying the *linear stability* of  $TW_m$ : the spatio-temporal voltage profile of an  $m$ -spike solution is determined by its firing functions,  $\tau$ , via (3.7); small perturbations  $\tau + \varphi$  to  $\tau$ , induce small perturbations to the spatio-temporal profile, and we expect that a suitable linearisation of the voltage mapping carries information concerning the asymptotic behaviour of these perturbations.

Building on the definitions and results in section 3, we have formalised the concept of linear stability, and developed an algorithm for  $TW_m$  linear stability computations. We give here a nontechnical summary of the main results, and we refer to the Supple-



mentary Material for a longer discussion including definitions, theorem statements, and proofs.

*Result 1 (Lemma D.1).* If two distinct  $m$ -spike solutions have firing functions  $\tau$  and  $\tau + \varphi$  then, to leading order,  $\varphi$  is in the kernel of a bounded linear operator,  $L: C_\eta(\mathbb{R}, \mathbb{R}^m) \rightarrow C_\eta(\mathbb{R}, \mathbb{R}^m)$ , obtained by linearising the voltage mapping  $V_m$  around  $\tau$ . We recall that  $\eta$  bounds the decay rate of the connectivity function,  $w \in L_\eta^1(\mathbb{R})$  (see Hypothesis 3.1). This implies that admissible perturbations  $\varphi$  are allowed to grow exponentially as  $|x| \rightarrow \infty$ , at a rate at most equal to the decay rate of  $w$ .

*Result 2 (Definition D.3 and surrounding discussion).* As for  $\text{TW}_m$  existence, linear stability is characterised via firing functions: loosely speaking, a wave with firing functions  $\tau$  is linearly stable to perturbations  $\varphi \in \ker L$  if the firing sets  $\mathbb{F}_\tau$  and  $\mathbb{F}_{\tau+\varphi}$  are close around  $t = 0$ , and remain close for all positive times (see also caption to Figure 6(c)).

*Result 3 (Lemma D.4 and following discussion).* Linear stability is determined by a complex-valued function  $E: \mathbb{D}_{-\eta, \eta} \rightarrow \mathbb{C}$ , where  $\mathbb{D}_{-\eta, \eta} = \{z \in \mathbb{C}: -\eta \leq \text{Re } z \leq \eta\}$ . A  $\text{TW}_m$  is stable to perturbations of the type  $\varphi(x) = \Phi e^{\lambda x} + \Phi^* e^{\lambda^* x}$  (where  $\Phi \in \mathbb{R}^m$  and the star denotes complex conjugation) if all nonzero roots  $\lambda$  of  $E$  have strictly negative real parts. The function  $E$  can be evaluated using the coarse wave variables  $(c, T)$ .

**5. Bifurcation structure of travelling waves.** The pseudo-arclength continuation routines developed in [70, 2] have been used to compute solutions to Problem 3.7, continue waves in parameter space, and investigate their stability. A  $\text{TW}_m$  is constructed by solving Problem 3.7 in the coarse variables  $(c, T) \in \mathbb{R}_{>0} \times \mathbb{R}^m$ , which is sufficient to reconstruct the wave profile (3.10), and the corresponding synaptic profile (3.11); in addition, starting from a solution to Problem 3.7, the linear asymptotic stability of a  $\text{TW}_m$  is determined by finding roots of the  $(c, T)$ -dependent nonlinear function  $E$  defined in (D.7).

Figure 7 shows the bifurcation structure of  $\text{TW}_3$ , which is common to most travelling waves found in the model. The simulations in Section 2 suggest to take the synaptic timescale parameter  $\beta$  as the principal continuation parameter. We use the wavespeed  $c$  as solution measure. A branch of solutions originates from a grazing point (G, see below for a more detailed explanation) and it is initially stable, before destabilising at a sequence of oscillatory bifurcations ( $\text{HB}_1$ – $\text{HB}_3$ ), as seen in Figure 7(a). In passing, we note that there exists a second, fully unstable, branch of  $\text{TW}_3$  solutions characterised by a slower speed and a smaller width. This branch, which we omit from the bifurcation diagrams for simplicity, also originates at a grazing point.

**5.1. Grazing points.** In a wide region of parameter space, branches of  $\text{TW}_m$  solutions originate at a grazing point  $\beta = \beta_G$ , as seen in Figure 7(a)–(b) for  $\text{TW}_3$ <sup>5</sup>. At a grazing point the  $\text{TW}_m$  profile crosses threshold  $m$  times, and attains the threshold tangentially at a further spatial location,  $cT_G$ , as shown in Figure 7(b). This tangency exists at the critical value  $\beta = \beta_G$ , signalling a non-smooth transition and a branch termination. For  $\beta > \beta_G$  we observe profiles with exactly  $m$  threshold crossings (a branch of  $\text{TW}_m$  solutions). These profiles exhibit a further local maximum, which is strictly less than 1 by construction, at a point  $\xi_{\max} > cT_m$ . As  $\beta \rightarrow \beta_G^+$ , we observe  $\xi_{\max} \rightarrow cT_G^+$  and  $\nu(\xi_{\max}) \rightarrow 1^-$ , until the threshold is reached at  $\beta = \beta_G$ , where the tangency originates.

<sup>5</sup>Note that  $\beta_G$  depend on  $m$ , but we omit this dependence to simplify notation. The same is true for other quantities in the paper such as  $c$  and  $T_G$ , for instance.

For  $\beta < \beta_G$ , we find solutions to the nonlinear problem (3.12)–(3.13) for which  $V_m\tau > 1$  in a bounded interval of  $\mathbb{R}$ . Since these states violate the condition (3.14), they do not correspond to  $TW_m$  solutions, and we disregard them (the branch terminates at  $\beta_G$ ). We note, however, that in a neighbourhood of  $\beta_G$  there exist branches of travelling wave solutions with different number of threshold crossings (as it will be shown below).

We found grazing points for every  $TW_m$  with  $2 \leq m \leq 230$ , for the parameters in Table 1 with  $d_1 = 0$ . We observe that for  $\beta < \beta_G$  the system evolves towards a DIFM bump attractor (see Figure 7(e)). Understanding the origin of this transition is the subject of the following sections.

Grazing points are found generically as a secondary control parameter is varied, and 2-parameter continuations of grazing points can be obtained numerically, by freeing one parameter and imposing tangency of the wave profile at one additional point (see Problem E.1 in Appendix E).

**5.2. Oscillatory bifurcations.** Along the  $TW_m$  branch, we compute and monitor the roots of  $E$  with the largest real part. Figure 7(c)–(d) show examples for  $TW_3$  at  $\beta = 10$  and  $\beta = 16$  respectively. At  $\beta = 10$ , we observe a root at 0, as expected, and other roots with small negative real part: the wave is therefore linearly asymptotically stable to firing-threshold perturbations  $x \mapsto \Phi e^{\lambda x} + \Phi^* e^{\lambda^* x}$ , with  $E(\lambda) = 0$  and  $\Phi \in \ker[D - M(\lambda)]$  (see Lemma D.4), as confirmed via simulation in Figure 7(f). In contrast, there exists a pair of unstable complex conjugate roots for the solution at  $\beta = 16$ , indicating an oscillatory (Hopf) instability, which is also confirmed by direct simulation, in Figure 7(g): after the initial oscillatory instability, the system destabilises to a  $TW_2$ . It should be noted that, in other regions of parameter space and for simulations with different network sizes, we observed a  $TW_3$  destabilise to a  $TW_1$  or the homogeneous steady state.

We expect that branches of periodically modulated  $TW_m$  solutions (which are also supported by neural fields [34, 25]) emerge from each of the Hopf bifurcations reported in Figure 7(a). We note that we could not find stable structures of this type via direct simulations near the onset of the instability, indicating that the Hopf bifurcations may be subcritical. While it is possible to extend our framework to continue such periodic states, we did not pursue this strategy here.

As shown in Figure 7(a), the  $TW_3$  branch undergoes a sequence of Hopf bifurcations  $\{\text{HB}_i\}_i$ : our stability analysis shows several pairs of complex conjugate roots progressively crossing the imaginary axis as  $\beta$  increases: the computation in Figure 7(d), for instance, is for a solution at  $\beta \in (\beta_{\text{HB}_1}, \beta_{\text{HB}_2})$ . We have verified numerically (not shown) that the firing functions of spatio-temporal DIFM solutions in this region of parameter behave as predicted by the leading eigenvalues in Figure 7(d), that is, they feature two dominant oscillatory modes: one stable, and one unstable. Similarly to grazing points, Hopf bifurcations can be continued in a secondary parameter (see Problem E.2 in Appendix E).

**5.3. Nested branches of travelling waves.** We computed branches of  $TW_m$  solutions for increasing values of  $m$ , as reported in Figure 8(a), using DIFM simulations as initial guesses. In Figure 1 waves were represented by their width, whereas here we use the propagation speed  $c$ . In the region of parameter space explored in the DIFM model, branches with  $m \geq 2$  feature a grazing point for low  $\beta$ , and branches with  $m \geq 3$  display sequences of Hopf Bifurcations, following the scenario already discussed in Figure 7(a). In this region, the  $TW_1$  branch has a distinct behaviour, featuring a saddle node point in place of a grazing point. For each  $TW_m$  branch ter-

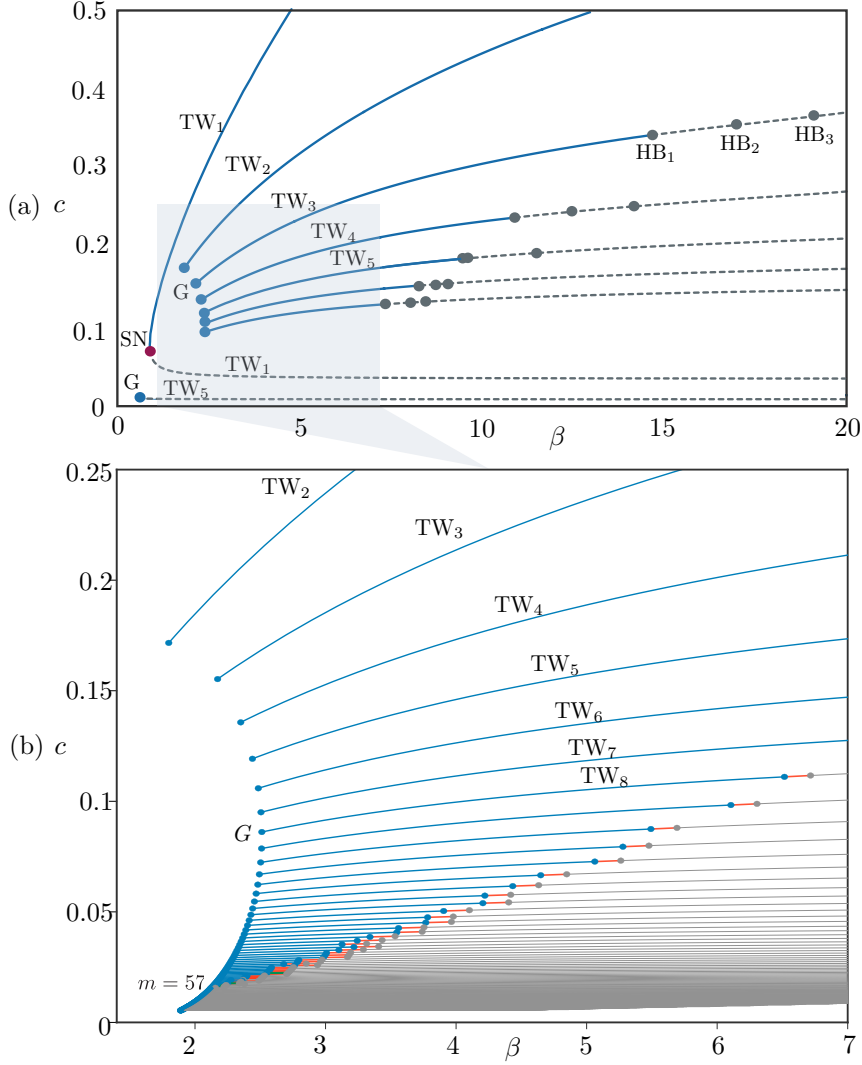


FIG. 8. Bifurcation structure of  $TW_m$  branches for  $m = 1, \dots, 160$  in the parameter  $\beta$ . (a): For  $m \geq 3$ , branches are similar to the one shown in Figure 7(a). As  $m$  increases, the waves become slower and their stability region narrower. The shaded area in (a) is enlarged in (b): the inset shows selected branches for  $m = 2, \dots, 160$ ; oscillatory instabilities occur within the red segments (connecting a stable solution in blue, to an unstable solution in grey), and the branches with  $m \geq 57$  are fully unstable (solid grey lines). We used here the same data as in Figure 1, but we present it in terms of  $c$ , not  $\Delta$ . Parameters as in Table 1, with  $d_1 = 0$ .

minating at a grazing point, there is a corresponding slow unstable branch originating at a different grazing point: in Figure 8(a) this behaviour is exemplified by plotting the fully unstable slow  $TW_5$  branch (the branch with slowest waves in the figure), but is omitted for all other branches. The two  $TW_5$  branches should be understood as a “broken saddle-node”. The bifurcation structure of Figure 8(a), valid for the CIFM, supports numerical simulations of the DIFM, in which a  $TW_m$  destabilises at  $HB_1$ , and gives rise to a new travelling wave state,  $TW_{m'}$  with  $m' < m$  (see for instance Figures 6 and 7).

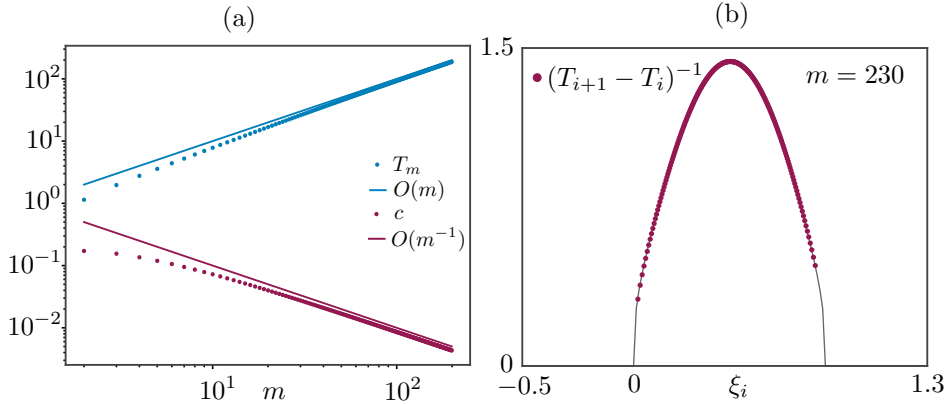


FIG. 9. (a) The quantities  $c$  and  $T_m$ , evaluated at the grazing points  $\beta = \beta_G$ , are  $O(m^{-1})$  and  $O(m)$ , respectively. Since  $T_1 = 0$  for all waves, the quantity  $cT_m$  measures the wave width, and we expect the sequence  $\{cT_m\}_{m \in \mathbb{N}}$ , the sequence of wave widths, to converge to a fixed value as  $m \rightarrow \infty$ . (b) The solid grey line is the spatial firing rate profile proposed in [56] for a non-wandering bump, red dots mark the instantaneous firing rate for  $TW_{230}$  at the grazing point, computed according to the formula  $(T_{i+1} - T_i)^{-1}$  at position  $x = cT_i$ .

These coexisting  $TW_m$  branches are nested in a characteristic fashion, so far unreported in the literature; the higher  $m$ , the slower the wave, and the narrower the stable interval between  $G$  and  $HB_1$ . This structure is noteworthy: firstly, it is known that the speed of  $TW_1$  typically changes as a secondary parameter is varied [32, 11, 12]; however, in networks with purely excitatory kernels, waves with multiple threshold crossings coexist, and their speed does not depend strongly on  $m$  [32], which has been a principle reason for studying approximately and analytically the only tractable case,  $m = 1$  [14, Section 5.4] (this scenario is also confirmed by our calculations, see Figure 13); secondly, it is known that Hopf instabilities with purely excitatory connectivity kernel are possible only if delays are present in the network [12].

The results in Figure 8 have been obtained using a methodology that works for arbitrary  $m$ , and on generic connectivity kernels. They show that, when inhibition is present: (i) coexisting nested branches of  $TW_m$  exist; (ii) the speed of such waves depends strongly on  $m$ , and in particular it is possible to construct waves with arbitrarily small speed, by increasing the number of spikes; (iii) oscillatory instabilities are present in models without delays, for sufficiently large  $m$  and/or sufficiently large  $\beta$ . As we shall see, the latter aspect plays a role in understanding the so called *bump attractor*.

**5.4. The bump attractor.** From the grazing point of  $TW_m$ , one can compute the grazing point of  $TW_{m+1}$ . For instance, from the  $TW_3$  grazing profile in Figure 7(b), we obtain  $(c, T_1, T_2, T_3, T_G)$ . A grazing point can then be computed solving Problem E.1, and its solution can be used to produce an initial guess  $(c, T_1, T_2, T_3, (T_3 + T_G)/2, T_G)$  for a grazing point of  $TW_4$ . Exploiting this iterative strategy, we compute grazing points and branches for large values of  $m$ , obtaining the diagram in Figure 8(b), corresponding to the shaded area in Figure 8(a).

The branches accumulate as  $m$  increases, and for  $m \geq 57$ , they are fully unstable for this parameter set. The diagrams provide evidence that there exist unstable waves with arbitrarily many spikes (i.e., with arbitrarily large  $m$ ) and vanishingly small speed. It seems therefore natural to postulate a relationship between these waves and

the bump structures found by Laing and Chow [56] (see also Figures 1, 3 and 7(e)).

**5.4.1. Spatial profile in non-wandering bumps.** In the CIFM, we inspected travelling wave profiles for  $TW_m$  solutions at each of the grazing points where they originate. The leftmost spike of each wave occurs at  $\xi_1 = 0$  by construction (see Problem 3.7), while its rightmost spike is at  $\xi_m = cT_m$ , which is therefore a proxy for the wave's width<sup>6</sup>. Figure 9(a) shows  $c$  and  $T_m$ , computed at the grazing points, as functions of  $m$ : we find  $c = O(m^{-1})$  and  $T_m = O(m)$ , therefore, we expect the sequence  $\{\xi_m\}_{m \in \mathbb{N}}$  to converge to a finite value  $\xi_*$  as  $m \rightarrow \infty$ .

These data indicate that, as the wavespeed tends to zero, the growing number of spikes are distributed in a fixed interval  $[0, \xi_*]$ . Hence, even though there exists no stationary and spatially heterogeneous CIFM solution for finite  $m$  (this possibility is ruled out by Definition 3.2), there is evidence that an  $m \rightarrow \infty$  limit of  $TW_m$  solutions exists, has 0 speed, and displays a spatially heterogeneous profile, localised in the region  $x \in [0, \xi_*]$ . Thus, the limiting state possesses features of the *stationary bumps* that are typically analysed in continuum neural field models.

To further substantiate this claim, we compare data of the slowest computed wave ( $TW_{230}$  at the grazing point) to data of a non-wandering bump in the DIFM. The DIFM also does not admit stationary spatially heterogeneous solutions, but supports non-wandering bump attractors (see Figure 3(a) and Figure 7(e) for examples). In such states, the dynamic is not stationary, with many asynchronous firing events occurring at microscopic level; Laing and Chow noted that this state has a spatially-dependent firing rate, for which they provide a closed-form expression. They also showed that their analytical prediction is in agreement with DIFM simulations of a non-wandering bump attractor; the firing rate profile is therefore a macroscopic observable of a non-wandering bump.

Figure 9(b) compares Laing and Chow's firing rate profile to the inverse interspike time  $1/(T_{i+1} - T_i)$  in the computed  $TW_{230}$ , that is, a proxy for the firing rate at  $x = \xi_i$ . The agreement is excellent, confirming that, from a macroscopic viewpoint, the DIFM bump attractors bear a strong relation to  $TW_m$  solutions in the limit of large  $m$ .

**5.4.2. Macroscopic observables of wandering bumps.** We further investigate the bump attractor state in relation to the  $TW_m$ , away from the non-wandering limit studied above: the analysis of the CIFM, in the region of parameter space where the bump attractor is observed, predicts the coexistence of the trivial attracting solution  $v(x, t) \equiv I$ , with arbitrarily slow, unstable waves whose spatial profile approximates that of a bump. Following the turbulence analogy, we provide evidence that transient states to the DIFM bump attractor, or the bump attractor itself, display features of the underlying unstable  $TW_m$ . We discuss data for three travelling wave observables: instantaneous speed, instantaneous width, and firing sets.

**Instantaneous speed and width.** We simulate the DIFM with  $n = 5,000$ , initialising the model from an unstable travelling wave of the CIFM,  $TW_{105}$ , and estimate the instantaneous speed  $c(t)$  of the numerical DIFM solution at  $q$  time points  $\{t_k : k \in \mathbb{N}_q\}$ , using a level set of the synaptic profile and finite differences, as follows:

$$z(t) = \max\{x \in \mathbb{S} : s(x, t) = 0.1\}, \quad c_k = (z(t_k) - z(t_{k-1})) / (t_k - t_{k-1}), \quad k \in \mathbb{N}_q.$$

A CIFM travelling wave solution corresponds to a constant  $c$ : when the DIFM solution displays a wave for large  $n$ , the sequence  $\{c_k\}_k$  converges to a constant value, if one

<sup>6</sup>Recall that  $c$  is also a function of  $m$ , but we omit this dependence for ease of notation.

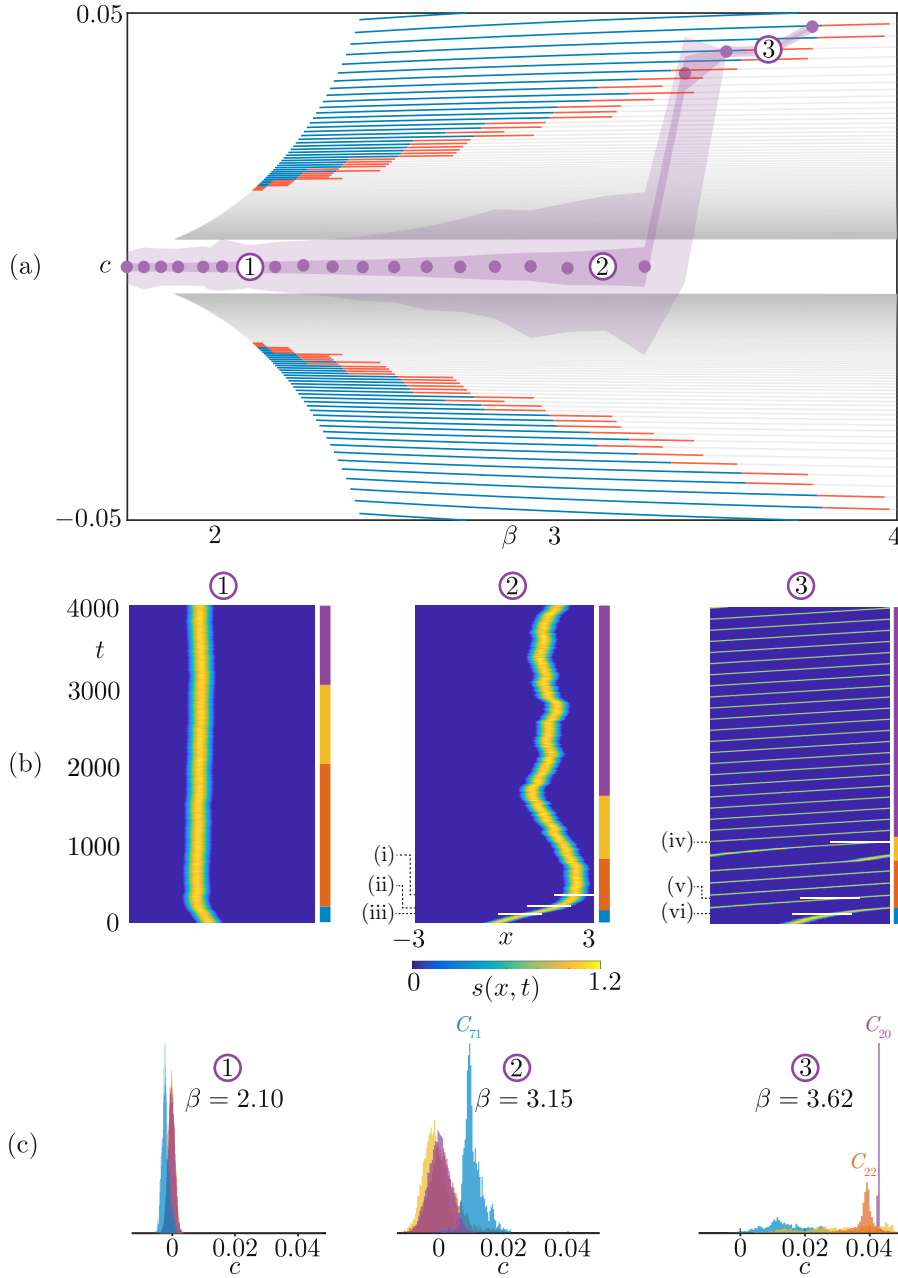


FIG. 10. (a): Mean instantaneous speed ( $\bar{c}$  in (5.1), purple dots) and interval estimators ( $[\bar{c} - \sigma_c, \bar{c} + \sigma_c]$  and  $[c_{min}, c_{max}]$ , dark and light purple shades, respectively) in direct simulations of the DIFM, superimposed on  $TW_m$  branches of the CIFM (an inset of Figure 8(b), which has been reflected about the  $c = 0$  axis to signpost waves with negative speed). The bump attractor is characterised by  $\bar{c} \approx 0$ , and fluctuations in speed that grow with  $\beta$ . (b): Exemplary solutions in (a) displaying an initial advection, followed by a bump attractor (1,2) or a stable wave (3). Snapshots of the rastergrams around times (i)–(vi) (white bars in the contour plots) are visible in Figure 11. (c) Histograms of the solution's instantaneous speed, computed in selected time intervals, indicated by blue, orange, yellow, and purple bars in (b). Sharp peaks indicate proximity of the orbit to a travelling wave, whose speed is indicated on top of the peaks ( $C_{71}$ ,  $C_{22}$ , and  $C_{20}$  for  $TW_{71}$ ,  $TW_{22}$ , and  $TW_{20}$ , respectively), see also Figure 11.

disregards small oscillations due to the finite  $n$ , and which vanish as  $n \rightarrow \infty$ . On the other hand, we expect that no differentiable function  $c(t)$  exists for a bump attractor. However, useful information may be found in the mean,  $\bar{c}$ , standard deviation,  $\sigma_c$ , and extrema,  $c_{\min}, c_{\max}$ , of the *deterministic* scalar  $c_k$

$$(5.1) \quad \bar{c} = \frac{1}{q} \sum_{k \in \mathbb{N}_q} c_k, \quad \sigma_c^2 = \frac{1}{q-1} \sum_{k \in \mathbb{N}_q} (c_k - \bar{c})^2, \quad c_{\min} = \min_{k \in \mathbb{N}_q} c_k, \quad c_{\max} = \max_{k \in \mathbb{N}_q} c_k.$$

These quantities are computed for long simulations (10,000 time units) after an initial transient (1,000 time units) for various values of  $\beta$ , and superimposed on the bifurcation diagram of the CIFM model, in [Figure 10\(a\)](#): we plot  $\bar{c}$  (purple dots) and two interval estimators,  $[\bar{c} - \sigma_c, \bar{c} + \sigma_c]$  (dark purple shade) and  $[c_{\min}, c_{\max}]$  (light purple shade). We recall that the CFIM admits branches of waves with positive and negative speed, both plotted in the figure, and that we omit slow unstable waves such as the one in [Figure 8\(a\)](#). Further, we conjectured above that branches of unstable waves also exist in the white band around  $c = 0$ .

[Figure 10](#) shows that the bump attractor dynamics with respect to the variable  $c(t)$  is confined to a region where unstable  $TW_m$  solutions exist for low and medium values of  $\beta$ . A similar behaviour is found for the instantaneous bump widths,  $\Delta(t)$ , which can also be estimated from  $z(t)$ . The macroscopic variable  $\Delta(t)$  does not have large variations within a bump attractor. As shown in [Figure 1](#), the average of  $\Delta(t)$  for a wandering bump attractor is located in the region of the bifurcation diagram where unstable  $TW_m$  are found.

For low and medium  $\beta$  values, we observe non-wandering and wandering bump attractors, albeit the fine details of the dynamics depend on initial conditions. [Figure 10\(b\)](#) shows 3 examples whose estimated average speeds appear also in [Figure 10\(a\)](#). The space-time plots display an initial advection, followed by a bump attractor, or a stable travelling wave. To gain insight into these transitions, we compute histograms of  $c_k$  in selected time intervals, indicated by blue, orange, yellow, and purple bars in [Figure 10\(b\)](#). Histograms that are sharply peaked around a nonzero value provide evidence that the solution spends time close to a wave. For instance, the purple histogram in [Figure 10\(c\)](#), orbit 3, has been computed on a long time interval signposted with a purple bar on the right vertical axis of [Figure 10\(b\)](#), orbit 3. The colormap of  $s(x, t)$  in [Figure 10\(b\)](#) shows that orbit 3 approaches a stable travelling wave, and the corresponding purple histogram is indeed close to a Dirac delta centred at  $C_{20}$ , the speed of the stable  $TW_{20}$ .

Before settling to  $TW_{20}$  the orbit spends time (orange bar in [Figure 10\(b\)](#), orbit 3) near the unstable  $TW_{22}$ : there is a clear transition in [Figure 10\(b\)](#), orbit 3 (after the orange bar), and the corresponding orange histogram has a tail, but is sharply peaked around  $C_{22}$ . This is in line with with the observation that  $c(t)$  has growing oscillations around  $C_{22}$ , and indeed  $TW_{22}$  is unstable. Similar considerations apply to [Figure 10\(b\)](#), orbit 2, which visits the unstable  $TW_{71}$ .

**Firing sets.** In addition to speed, we compare the firing sets of solutions labelled 2 and 3 in [Figure 10](#) to the ones of selected  $TW_m$ . The former are transient solutions, the latter are invariant, and we overlay them in [Figure 11](#). The firing set of solution 3 around the time labelled (iv) [Figure 10\(b\)](#) is visible in [Figure 11\(iv\)](#). From the initial condition at  $TW_{105}$ , propagating with positive speed, the solution slows down and ‘‘sheds’’ firing functions to the right of the profile, while the travelling firing set at the core persists to oscillatory perturbations. For a visual comparison with CIFM waves, we overlay in [Figure 11\(iv\)](#) a  $TW_{71}$  solution with a propagation speed close to

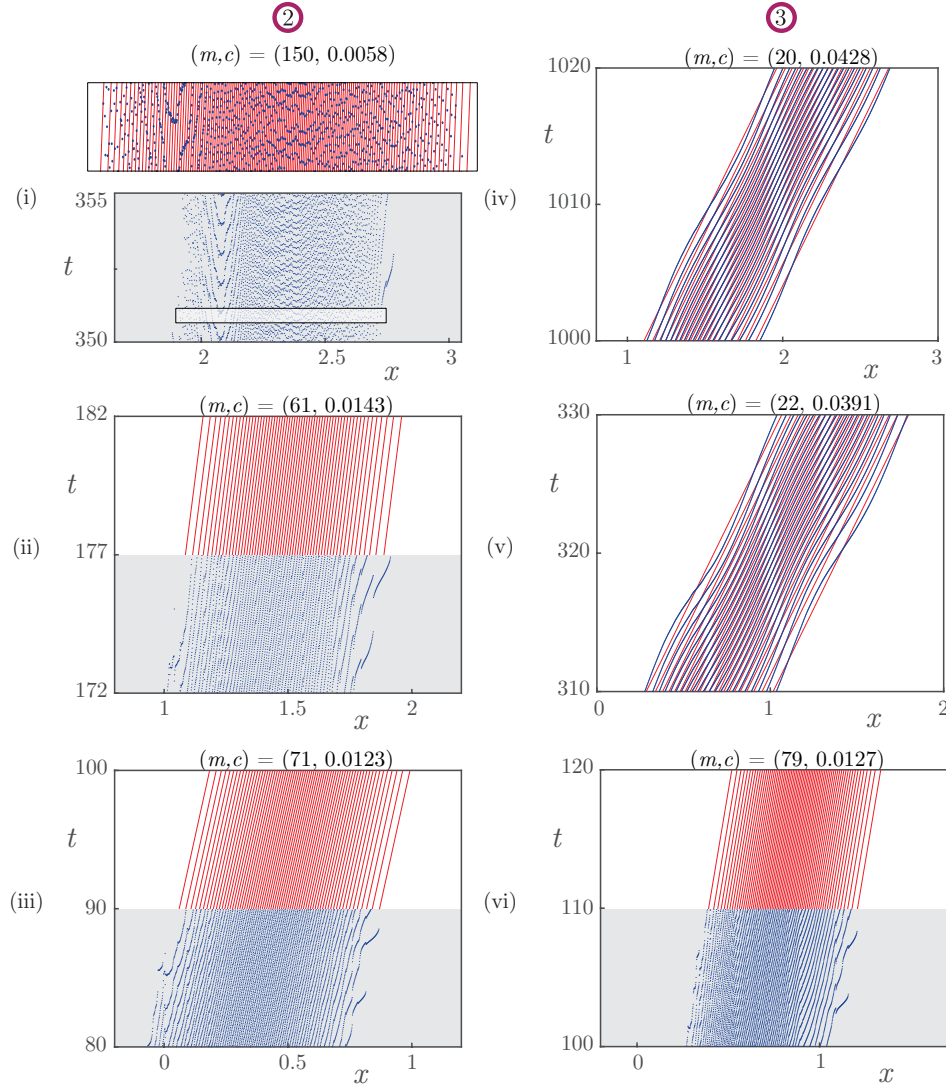


FIG. 11. Firing set of the DIFM solutions (blue dots) and of selected CIFM waves (overlaid red lines, with corresponding values of  $m$  and  $c$  near the times marked with a white tick (i)–(vi) in Figure 11(b)). The firing set (vi) of orbit (3) has a recognisable travelling core which progressively loses firing functions at the edges, until it visits the weakly unstable  $TW_{22}$  and is attracted to the stable  $TW_{20}$ . The same initial condition with a different  $\beta$  value leads to orbit (2). The firing sets (ii) and (iii) are qualitatively similar to (vi). The chaotic bump attractor (i) has distinctive travelling firing sets at the edges, visible in the grey raster plot: firing lines are lost to the right, and new travelling lines are injected into the core from the left, through a repeating V-shaped pattern.

the transient. After this strongly nonlinear transient, the solution visits the weakly unstable  $TW_{22}$ : in this transient, the firing set of the DIFM solution clearly displays the oscillations predicted by the linear stability theory for  $TW_{22}$  (see Figure 11(v)), before losing 2 further firing curves and being attracted to the stable  $TW_{20}$  (see Figure 11(iv) and the purple, sharply peaked histogram in Figure 10(c), label 3).



Solutions 2 and 3 in [Figure 10\(b\)](#) both start from  $TW_{105}$ , and the latter displays a similar transient dynamics to the former, with a travelling core and progressive loss of firing functions ([Figure 11\(ii\)–\(iii\)](#)), accompanied by an increase in propagation speed. The bump attractor alternates phases with small negative and positive propagation speed, as in [Figure 11](#). As expected, it is challenging to single out a matching wave in this highly chaotic regime, albeit we present a comparison with  $TW_{150}$ . The bump still features distinctive travelling firing sets at the edges, visible in the grey raster plot. The right edge has a marked alignment of firing events, and some firing curves terminate as in the other figures. Meanwhile, new firing curves are injected into the core from the left, through a characteristic, repeated V-shaped pattern. When the bump attractor propagates slowly with negative speeds, the V-shaped patterns are on the right, and firing lines are shed on the left (not shown).

**5.5. Composite waves.** In addition to the waves studied thus far, we found by direct simulation waves whose firing functions are split into well-separated groups, that is, firing functions in the same group are closer to each other than they are to those in other groups, see [Figure 12](#). We call these structures *composite waves*, as they may be formed via the interaction of travelling waves with various numbers of spikes. As in other non-smooth dynamical systems [\[46\]](#), we expect that these solutions have discontinuities that are rearranged with respect to a  $TW_m$ .

For illustrative purposes, we denote a composite wave with  $k \in \mathbb{N}$  groups by  $TW_{m_1} + \dots + TW_{m_k}$ , where  $\{m_i\}_{i=1}^k$  is a sequence of positive integers specifying the number of spikes in each group. There are constraints for the groups, dictated by dynamical considerations: for instance a  $TW_1 + TW_3$  cannot exist, because a  $TW_1$ , taken in isolation, is faster than a  $TW_3$ . The construction of asymptotic profiles and computation of linear stability for composite waves follow in the same way as defined in [section 3](#) and [section 4](#).

In [Figure 12\(a\)](#), we show a selection of composite waves near the  $TW_3$  branch. Roughly speaking, the wave profile along each depicted branch comprises a  $TW_3$  as its leading group, followed by two additional spike group that collectively form a compound satisfying the travelling wave conditions (e.g., branch 1 combines a  $TW_3$ , a  $TW_2$  and a  $TW_1$ ). The branches of composite waves are separate from each other and from the previously computed  $TW_m$  branches in [Figure 8](#), however, all branches possess a bifurcation structure similar to the one of the  $TW_m$  discussed in the past section. Moreover, we see that the magnitude of the speed of the composite wave is bounded above by the magnitude of the speed of the group at the leading edge of the wave (the slowest wave,  $TW_3$  in this case).

Direct numerical simulation highlights that composite waves can be formed from the interaction of multi-spike waves as shown in the left panel of [Figure 12\(b\)](#). Here we choose an initial condition with well separated  $TW_1$ ,  $TW_2$  and  $TW_3$  profiles. Initially, these separated structures travel with different speeds ( $TW_1$  being the fastest and  $TW_3$  the slowest, in line with what was found in [Figure 8\(a\)](#)). After a transient, the waves come closer and form a compound (the composite wave), with a common intermediate speed. The dynamics of composite waves depend greatly on the initial conditions: in the right panel of [Figure 12\(b\)](#), we see that an initial condition in which a  $TW_1$  lies between another  $TW_1$  and a  $TW_3$  leads to the extinction of the intermediate wave resulting in a composite wave with a total of 4 spikes.

Composite waves can also result from the collision between waves and wandering bumps ([Figure 12\(c\)](#), left panel). Here, we see a transition of two bump states into a composite wave that is compounded with a pre-existing  $TW_5$ . The interaction with

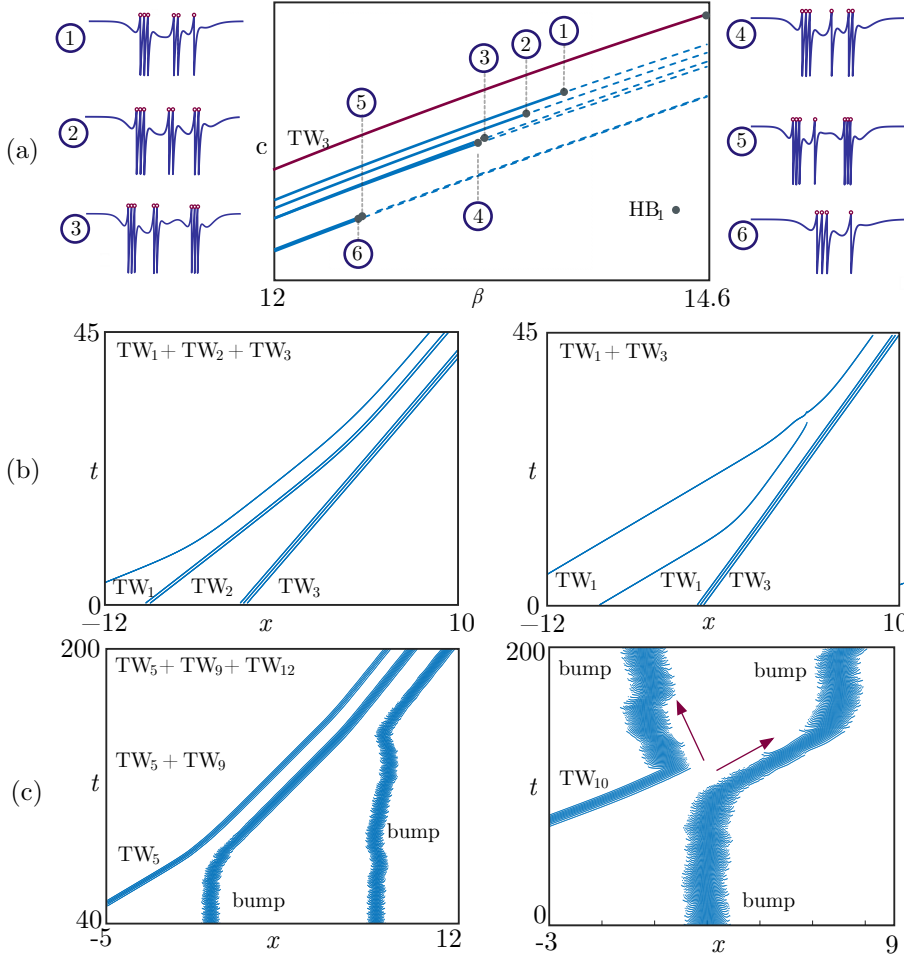


FIG. 12. (a) Bifurcation diagram of selected composite waves. The red curve is a  $TW_3$  branch, as computed in Figure 7. The blue curves are branches of composite waves, featuring an approximate  $TW_3$  at the front of the wave. The composite waves are slightly slower than  $TW_3$ . The diagram shows selected profiles at the first oscillatory bifurcation points. (b) Examples of composite waves obtained via collisions of multi-spike waves. (c) Collisions between  $m$ -spike propagating structures and wandering bumps generate composite waves (left) or bump repulsion (right), depending on initial conditions. Simulations in panels (b)–(c) have a lattice spacing of  $\Delta x = 2L/n = 0.01$ .

the  $TW_5$  causes the left-most bump to visit the branches of travelling wave solutions whereupon the combined state settles on a stable  $TW_5 + TW_9$ . This process is repeated for the right-most bump, giving rise to an overall  $TW_5 + TW_9 + TW_{12}$ . In the right panel of the Figure 12(c), we see that the same kind of collision can instead result in the wave packet transitioning to a wandering bump itself, highlighting the dependence of the formation of composite waves on initial conditions. In this scenario, the bump state does not visit a stable travelling wave branch and so only transiently adopts a weakly unstable wave profile before returning to a bump attractor state.

**6. Conclusions.** We have provided evidence that the relationship between bump attractors and travelling waves in a classical network of excitable, leaky integrate-and-fire neurons bears strong similarities to the one between complex spatiotemporal

patterns and waves at the onset of pipe turbulence. We made analytical and numerical progress in the construction and stability analysis of travelling waves with a large number of localised spikes, and gained access to their intricate bifurcation structure. This step was essential, because such waves advect, at low speed, localised patterns that resemble the bump attractor core. It should be noted that the waves we computed are only a subset of the ones supported by the model.

As we completed the present paper, a recent publication [57] reported the existence of waves with vanishingly small speed, and discontinuous profiles, in networks of theta neurons, which can be cast as spiking networks with a polynomial ODE of quadratic type. A natural question arises as to whether the fluid-dynamical analogy applies in that and other network models. The level-set approach used in the present paper was particularly effective because one can define  $m$ -spike waves starting from mild solutions to the formal evolution equation (3.1), and derive a relatively simple expression for the wave profile (3.10). While this approach may be harder to carry out in more detailed spiking models, the general idea of a relationship between localised waves and bumps in spiking networks could be investigated, by direct simulations, in more realistic networks (spiking or not).

An important open question concerns the definition of (3.1) and, more generally, of spatially-continuous spiking networks, as dynamical systems posed on function spaces. This problem has been circumvented here by defining a suitable class of solutions, introducing the voltage mapping, and then providing proofs of its relevance to the construction and stability of multiple-spike waves. We believe that a full dynamical-systems characterisation of similar models will be a key ingredient to uncover further links between localised waves and bumps in complex, spatially-extended threshold networks.

**Acknowledgments.** We are grateful to Stephen Coombes, Predrag Cvitanović, Gregory Faye, Joel Feinstein, John Gibson, Joost Hulshof, Rich Kerswell, and Edgar Knobloch for insightful discussions.

TABLE 1

*Parameter descriptions and nominal values for the Discrete Integrate-and-Fire Model.*

Parameter	Symbol	Value(s)
Number of neurons	$n$	{80,500,1000,5000}
Domain half-width	$L$	{1,3,4}
Synaptic efficacy and time scale	$\beta$	[0,25]
Synaptic excitation coefficient	$a_1$	11
Synaptic inhibition coefficient	$a_2$	7
Synaptic excitation spatial scale	$b_1$	5
Synaptic inhibition spatial scale	$b_2$	3.5
Constant external input	$I$	0.9
Time-dependent external input duration	$\tau_{\text{ext}}$	2
Time-dependent external input strength	$d_1$	{0,2}
Time-dependent external input spatial scale	$d_2$	{10,12}

**Appendix A. Synaptic, Reset, and Voltage mappings.** The following lemma shows that the synaptic contribution is a continuous function on the plane, hence discontinuities in the voltage come through the reset operator, as expected. It also provide domains and codomains for the Synaptic, Reset, and Voltage mappings.

LEMMA A.1. *If Hypothesis 3.1 holds, then for the operators  $S, R$  in Definition 3.3 we have  $S: C(\mathbb{R}) \rightarrow BC(\mathbb{R}^2)$  and  $R: C(\mathbb{R}) \rightarrow B(\mathbb{R}^2)$ , respectively.*

*Proof.* Fix  $u \in C(\mathbb{R})$ . The real-valued function  $z \mapsto \exp(-z)H(z)$  is bounded in  $\mathbb{R}$ , hence  $Ru \in B(\mathbb{R}^2)$ . To prove the result on  $S$ , we define the functions

$$\psi(y, t) = \int_{-\infty}^t e^{z-t} \alpha(z - u(y)) dz, \quad s(x, t) = (Su)(x, t) = \int_{-\infty}^{\infty} w(x - y) \psi(y, t) dy,$$

and set  $K_\alpha = \|\alpha\|_\infty$ ,  $K_w = \|w\|_{L^1(\mathbb{R})}$ , whose existence is guaranteed by Hypothesis 3.1. The function  $s$  is bounded on  $\mathbb{R}^2$  because  $|\psi| \leq K_\alpha$  on  $\mathbb{R}^2$ , hence

$$|s(x, t)| \leq K_\alpha \int_{-\infty}^{\infty} |w(x - y)| dy \leq K_\alpha K_w.$$

In order to prove the continuity of  $s$ , it is useful to first show that  $\psi$  is continuous in  $t$  on  $\mathbb{R}$ , uniformly in  $y$ . This claim is proved by noting that, for any  $y, t, \tau \in \mathbb{R}$  with  $t < \tau$  we have

$$\begin{aligned} |\psi(y, \tau) - \psi(y, t)| &= \left| \int_{-\infty}^t [e^{z-\tau} - e^{z-t}] \alpha(z - u(y)) dz + \int_t^\tau e^{z-\tau} \alpha(z - u(y)) dz \right| \\ &\leq K_\alpha \int_{-\infty}^t e^{z-t} - e^{z-\tau} dz + K_\alpha (\tau - t) \\ &= K_\alpha (1 - e^{-(\tau-t)} + \tau - t), \end{aligned}$$

which, combined with a similar argument for  $\tau < t$ , leads to

$$(A.1) \quad |\psi(y, \tau) - \psi(y, t)| \leq K_\alpha (1 - e^{-|\tau-t|} + |\tau - t|), \quad \text{for all } y, t, \tau \in \mathbb{R}.$$

We prove the continuity of  $s$  by showing that  $|s(\xi, \tau) - s(x, t)| \rightarrow 0$  as  $(\xi, \tau) \rightarrow (x, t)$ . We consider the following inequality

$$(A.2) \quad |s(\xi, \tau) - s(x, t)| \leq |s(\xi, \tau) - s(x, \tau)| + |s(x, \tau) - s(x, t)|,$$

and we note that the second term in the right-hand side of (A.2) can be made arbitrarily small as  $(\xi, \tau) \rightarrow (x, t)$ , owing to (A.1). Therefore it suffices to show that the first term in the right-hand side of (A.2) can also be made arbitrarily small as  $(\xi, \tau) \rightarrow (x, t)$ , that is, we must show that for any  $\varepsilon > 0$  there exists  $\delta > 0$  such that  $|s(\xi, \tau) - s(x, \tau)| < \varepsilon$ . To prove this statement, we use the boundedness of  $\psi$  and a change of variables in the integral to obtain the estimate

$$\begin{aligned} |s(\xi, \tau) - s(x, \tau)| &\leq \int_{-\infty}^{\infty} |w(y - \xi) - w(y - x)| |\psi(y, \tau)| dy \\ &\leq K_\alpha \int_{-\infty}^{\infty} |w(y + x - \xi) - w(y)| dy, \end{aligned}$$

therefore, for any  $X > 0$  we have

$$\begin{aligned} |s(\xi, \tau) - s(x, \tau)| &\leq K_\alpha \int_{-\infty}^{-X} |w(y + x - \xi) - w(y)| dy \\ &\quad + K_\alpha \int_{-X}^X |w(y + x - \xi) - w(y)| dy \\ &\quad + K_\alpha \int_X^{\infty} |w(y + x - \xi) - w(y)| dy := K_\alpha (I_1 + I_2 + I_3). \end{aligned}$$

We bound  $I_3$  as follows

$$\begin{aligned} I_3 &\leq \int_X^\infty |w(y+x-\xi)| dy + \int_X^\infty |w(y)| dy \\ &= \int_{X+x-\xi}^\infty |w(y)| dy + \int_X^\infty |w(y)| dy \leq 2 \int_{X-|x-\xi|}^\infty |w(y)| dy \end{aligned}$$

and a similar reasoning gives an identical bound for  $I_1$ ,

$$I_1 \leq 2 \int_{X-|x-\xi|}^\infty |w(y)| dy.$$

We conclude that, for any  $X > 0$

$$|s(\xi, \tau) - s(x, \tau)| \leq 4K_\alpha \int_{X-|x-\xi|}^\infty |w(y)| dy + K_\alpha \int_{-X}^X |w(y+x-\xi) - w(y)| dy.$$

We now fix  $\varepsilon, \delta_1 > 0$ . Since  $w \in L^1(\mathbb{R})$ , we can pick  $X$  so that

$$|x - \xi| < \delta_1 \quad \Rightarrow \quad 4K_\alpha \int_{X-|x-\xi|}^\infty |w(y)| dy < \frac{\varepsilon}{2}.$$

Furthermore, by continuity of  $w$  there exists  $\delta_2 > 0$  such that

$$|x - \xi| < \delta_2 \quad \Rightarrow \quad K_\alpha \int_{-X}^X |w(y+x-\xi) - w(y)| dy \leq \frac{\varepsilon}{2},$$

hence for any  $\varepsilon > 0$  there exists  $\delta = \min(\delta_1, \delta_2) > 0$  such that  $|s(\xi, \tau) - s(x, \tau)| < \varepsilon$ , which implies the continuity of  $s$ . We conclude that  $S: C(\mathbb{R}) \rightarrow BC(\mathbb{R}^2)$ .  $\square$

**Appendix B. Discontinuities of  $v_m$ .** In some cases it is useful to replace the threshold conditions (3.3) and (3.8) by equivalent conditions involving left limits of the voltage function and mapping, respectively, as specified by the following result.

**COROLLARY B.1** (Discontinuities of  $v_m$ ). *Under the hypotheses of Lemma A.1,  $v_m = 1$  in  $\mathbb{F}_\tau$  if, and only if,  $\lim_{\mu \rightarrow 0^+} v_m(x, \tau_i(x) - \mu) = v_m(x, \tau_i(x)^-) = 1$  for all  $(i, x) \in \mathbb{N}_m \times \mathbb{R}$ .*

*Proof.* The condition  $v_m(x, t) = 1$  for  $(x, t) \in \mathbb{F}_\tau$  is equivalent to

$$v_m(x, \tau_i(x)) = 1 \quad (i, x) \in \mathbb{N}_m \times \mathbb{R}.$$

From the definitions of  $S$  and  $R$ , and the continuity  $S\tau_i$  on  $\mathbb{R}^2$  (see Lemma A.1) we have, for all  $(i, x) \in \mathbb{N}_m \times \mathbb{R}$

$$\begin{aligned} v_m(x, \tau_i(x)) &= I + \sum_{j \in \mathbb{N}_m} (S\tau_j)(x, \tau_i(x)) - \sum_{j < i} \exp(\tau_j(x) - \tau_i(x)) \\ &= I + \sum_{j \in \mathbb{N}_m} \lim_{\mu \rightarrow 0^+} (S\tau_j)(x, \tau_i(x) - \mu) - \sum_{j < i} \exp(\tau_j(x) - \tau_i(x)) \\ &= I + \lim_{\mu \rightarrow 0^+} \sum_{j \in \mathbb{N}_m} \left[ (S\tau_j)(x, \tau_i(x) - \mu) - (R\tau_j)(x, \tau_i(x) - \mu) \right] = v_m(x, \tau_i(x)^-), \end{aligned}$$

hence  $v_m = 1$  in  $\mathbb{F}_\tau$  if, and only if,  $v_m(x, \tau_i(x)^-) = 1$  for all  $(i, x) \in \mathbb{N}_m \times \mathbb{R}$ .  $\square$

### Appendix C. Proof of Proposition 3.6.

PROPOSITION C.1 (TW<sub>m</sub> profile). A TW<sub>m</sub> with speed  $c$  satisfies  $(V_m\tau)(x, t) = \nu_m(ct - x; c, T)$ , and its  $(c, T)$ -dependent travelling wave profile  $\nu_m$  is given by

$$(C.1) \quad \begin{aligned} \nu_m(\xi; c, T) = I - \sum_{j \in \mathbb{N}_m} \exp\left(-\frac{\xi - cT_j}{c}\right) H\left(\frac{\xi - cT_j}{c}\right) \\ + \frac{1}{c} \sum_{j \in \mathbb{N}_m} \int_{-\infty}^{\xi} \exp\left(\frac{z - \xi}{c}\right) \int_0^{\infty} w(y - z + cT_j) p(y/c) dy dz. \end{aligned}$$

*Proof.* We set  $\tau_j(x) = x/c + T_j$  for  $j \in \mathbb{N}_n$ . The first sum in (C.1) is immediate, as

$$(R\tau_j)(x, t) = \exp\left(\frac{cT_j - ct + x}{c}\right) H\left(\frac{ct - x - cT_j}{c}\right)$$

The second sum is obtained as follows:

$$\begin{aligned} (S\tau_j)(x, t) &= \int_{-\infty}^t \int_{-\infty}^{\infty} \exp(s - t) w(x - y) \alpha(s - \tau_j(y)) dy ds \\ &= \int_{-\infty}^t \int_0^{\infty} \exp(s - t) w(x + y - cs + cT_j) p(y/c) dy ds \\ &= \frac{1}{c} \int_{-\infty}^{ct-x} \int_0^{\infty} \exp\left(\frac{s + x - ct}{c}\right) w(y - s + cT_j) p(y/c) dy ds. \quad \square \end{aligned}$$

### Appendix D. Travelling wave stability.

We begin by showing that if two distinct  $m$ -spike solutions have firing functions  $\tau$  and  $\tau + \varphi$ , respectively, then the perturbations  $\varphi$  satisfy a linear equation to leading order. The following lemma also specifies admissible perturbations, namely  $\varphi$  are in the Banach space  $C_\eta(\mathbb{R}, \mathbb{R}^m)$ : perturbations are allowed to grow exponentially as  $|x| \rightarrow \infty$ , at a rate at most equal to  $\eta$ , which bounds the decay rate of the connectivity kernel function  $w \in L_\eta^1(\mathbb{R})$ .

LEMMA D.1 (Linearisation of the voltage mapping operator). *Assume Hypothesis 3.1, and let  $(c, T)$  be the coarse variables of a TW<sub>m</sub> with firing functions  $\tau$ . Further, let  $L$  be the linear operator defined by  $L\varphi = ((L\varphi)_1, \dots, (L\varphi)_m)$ , where*

$$(L\varphi)_i = \sum_{j \in \mathbb{N}_m} (\varphi_i - \varphi_j) 1_{j < i} + \int_{cT_{j_i}}^{\infty} e^{-y/c} w(y) \psi_{ij}(y) [\varphi_i - \varphi_j(\cdot - y)] dy, \quad i \in \mathbb{N}_m,$$

with coefficients  $T_{ij}$  and functions  $\psi_{ij}$  given by

$$T_{ij} = T_i - T_j, \quad \psi_{ij}: [cT_{ij}, \infty) \rightarrow \mathbb{R}, \quad y \mapsto p(0) + \int_0^{y/c - T_{j_i}} e^s p'(s) ds, \quad i, j \in \mathbb{N}_n,$$

respectively. The following statements hold:

1.  $L$  is a bounded operator from  $C_\eta(\mathbb{R}, \mathbb{C}^m)$  to itself.
2. Let  $0 < \varepsilon \ll 1$  and  $\varphi \in C_\eta(\mathbb{R}, \mathbb{R}^m)$ . If  $\tau + \varepsilon\varphi$  are firing functions of an  $m$ -spike CIFM solution (a perturbation of the TW<sub>m</sub>), then

$$(D.1) \quad 0 = L\varphi + O(\varepsilon) \quad \text{in } \mathbb{R}$$

*Proof. Part 1.* If  $\varphi \in C_\eta(\mathbb{R}, \mathbb{C}^m)$ , then  $\varphi \in C(\mathbb{R}, \mathbb{C}^m)$  and  $L\varphi \in C(\mathbb{R}, \mathbb{C}^m)$ . We show that for any  $\varphi \in C_\eta(\mathbb{R}, \mathbb{C}^m)$  there exists a positive constant  $\kappa_{m,\eta}$  such that  $\|L\varphi\|_{C_{m,\eta}} \leq \kappa_{m,\eta}\|\varphi\|_{C_{m,\eta}}$ , which implies that  $L$  is a bounded operator from  $C_\eta(\mathbb{R}, \mathbb{C}^m)$  to itself. We begin by estimating  $\psi_{ij}$ : by [Hypothesis 3.1](#) there exist constants  $K_p, K_{p'}$  such that

$$\begin{aligned} |\psi_{ij}(y)| &\leq |p(0)| + \int_0^{y/c-T_{ji}} e^z |p'(z)| dz \\ &\leq K_p + K_{p'} \int_0^{y/c-T_{ji}} e^z dz = K_p + K_{p'}(e^{y/c-T_{ji}} - 1), \end{aligned}$$

therefore, introducing the constant  $K = 2 \max(K_p, K_{p'}) \max_{i,j} e^{-T_{ji}}$ ,

$$(D.2) \quad e^{-y/c} |\psi_{ij}(y)| \leq e^{-y/c} (K_p + K_{p'} e^{y/c-T_{ji}}) \leq K$$

uniformly in  $(i, j, y) \in \mathbb{N}_m \times \mathbb{N}_m \times [cT_{ji}, \infty)$ .

We now fix  $\varphi \in C_\eta(\mathbb{R}, \mathbb{C}^m)$ ,  $x \in \mathbb{R}$ , and estimate

$$(D.3) \quad \begin{aligned} |(L\varphi)(x)|_\infty &\leq \max_{i \in \mathbb{N}_m} \sum_{j \in \mathbb{N}_m} (|\varphi_i(x)| + |\varphi_j(x)|) \\ &\quad + \max_{i \in \mathbb{N}_m} \sum_{j \in \mathbb{N}_m} \int_{cT_{ji}}^\infty e^{-y/c} |w(y)\psi_{ij}(y)| |\varphi_i(x) - \varphi_j(x-y)| dy. \end{aligned}$$

For the first summands in [\(D.3\)](#) we find

$$(D.4) \quad |\varphi_i(x)| + |\varphi_j(x)| \leq 2|\varphi(x)|_\infty \leq 2e^{\eta|x|} \|\varphi\|_{C_{m,\eta}}$$

For the second summands in [\(D.3\)](#), we estimate

$$(D.5) \quad \begin{aligned} &\int_{cT_{ji}}^\infty e^{-y/c} |w(y)\psi_{ij}(y)| |\varphi_i(x) - \varphi_j(x-y)| dy && \text{(by (D.2))} \\ &\leq K \int_{cT_{ji}}^\infty |w(y)| |\varphi_i(x) - \varphi_j(x-y)| dy \\ &\leq K \|\varphi\|_{C_{m,\eta}} \int_{cT_{ji}}^\infty |w(y)| (e^{\eta|x|} + e^{\eta|x-y|}) dy \\ &\leq K e^{\eta|x|} \|\varphi\|_{C_{m,\eta}} \int_{cT_{ji}}^\infty |w(y)| (1 + e^{\eta|y|}) dy \\ &\leq K e^{\eta|x|} \|\varphi\|_{C_{m,\eta}} \left( \|w\|_{L_\eta^1} + \int_{cT_{ji}}^\infty |w(y)| e^{\eta|y|} dy \right) && (w \text{ even}) \\ &\leq K e^{\eta|x|} \|\varphi\|_{C_{m,\eta}} \left( \|w\|_{L_\eta^1} + 2 \int_{-\infty}^\infty |w(y)| e^{\eta y} dy \right) \\ &\leq 3K \|w\|_{L_\eta^1} e^{\eta|x|} \|\varphi\|_{C_{m,\eta}} \end{aligned}$$

Combining [\(D.3\)](#)–[\(D.5\)](#) we obtain

$$\begin{aligned} \|L\varphi\|_{C_{m,\eta}} &= \sup_{x \in \mathbb{R}} e^{-\eta|x|} |L\varphi(x)|_\infty \\ &\leq m(2 + 3K \|w\|_{L_\eta^1}) \|\varphi\|_{C_{m,\eta}} := \kappa_{m,\eta} \|\varphi\|_{C_{m,\eta}}, \end{aligned}$$

which concludes the proof of part 1.

*Part 2.* We set  $u = \tau + \varepsilon\varphi \in C_\eta(\mathbb{R}, \mathbb{R}^m)$ , for  $0 < \varepsilon \ll 1$ . By main hypothesis  $u$  and  $\tau$  are firing functions of two distinct  $m$ -spike CIFM solutions. We claim that this implies Equation (D.1). Indeed, since  $u$  is a firing function, then  $V_m u = 1$  on  $\mathbb{F}_u$ , that is

$$(D.6) \quad 1 = I + \sum_{j \in \mathbb{N}_m} \left( (Su_i)(x, u_j(x)) + (Ru_j)(x, u_i(x)) \right), \quad (i, x) \in \mathbb{N}_m \times \mathbb{R}.$$

We obtain

$$\begin{aligned} (Su_j)(\cdot, u_i) &= \int_{-\infty}^{\infty} w(\cdot - y) \int_{-\infty}^0 e^z \alpha(z + u_i - u_j(y)) dz dy \\ &= (S\tau_j)(\cdot, \tau_i) + \varepsilon \int_{-\infty}^{\infty} w(\cdot - y) (\varphi_i - \varphi_j(y)) \int_{-\infty}^0 e^z \alpha'(z + \tau_i - \tau_j(y)) dz dy \\ &\quad + O(\varepsilon^2), \end{aligned}$$

where we have denoted by  $\alpha' = p'H + p\delta$  the distributional derivative of  $\alpha$ . We now manipulate the integral in the previous equation as follows

$$\begin{aligned} &\int_{-\infty}^{\infty} w(\cdot - y) (\varphi_i - \varphi_j(y)) \int_{-\infty}^0 e^z \alpha'(z + \tau_i - \tau_j(y)) dz dy \\ &= \int_{-\infty}^{\infty} w(\cdot - y) (\varphi_i - \varphi_j(y)) \int_{-\infty}^{\tau_i - \tau_j(y)} e^{z + \tau_i - \tau_j(y)} \alpha'(z) dz dy \\ &= \int_{-\infty}^{\infty} w(\cdot - y) (\varphi_i - \varphi_j(y)) \int_{-\infty}^{\tau_i - \tau_j(y)} e^{z + \tau_i - \tau_j(y)} (p'(z)H(z) + p(z)\delta(z)) dz dy \\ &= \int_{-\infty}^{\tau_j^{-1}(\tau_i)} w(\cdot - y) (\varphi_i - \varphi_j(y)) e^{\tau_j(y) - \tau_i} \left( p(0) + \int_0^{\tau_i - \tau_j(y)} e^z p'(z) dz \right) dy \end{aligned}$$

hence for all  $i, j \in \mathbb{N}_m$  we obtain

$$(Su_j)(\cdot, u_i) = (S\tau_j)(\cdot, \tau_i) + \varepsilon e^{T_{ji}} \int_{-\infty}^{\infty} e^{-y/c} w(y) \psi_{ij}(y) [\varphi_i - \varphi_j(\cdot - y)] dy + O(\varepsilon^2)$$

For the reset operator, we obtain, for all  $i, j \in \mathbb{N}_m$

$$\begin{aligned} Ru_j(\cdot, u_i^-) &= - \lim_{\kappa \rightarrow 0^+} \exp(-u_i + \kappa + u_j) H(u_i - \kappa - u_j) \\ &= R\tau_j(\cdot, \tau_i^-) + \varepsilon \lim_{\kappa \rightarrow 0^+} \exp(-T_{ij} + \kappa) (\varphi_i - \varphi_j) H(T_{ij}) + O(\varepsilon^2) \\ &= R\tau_j(\cdot, \tau_i^-) + \varepsilon \exp(T_{ji}) (\varphi_i - \varphi_j) 1_{j < i} + O(\varepsilon^2). \end{aligned}$$

Combining (D.6) with the expansions obtained for  $S$  and  $R$ , exploiting the condition  $V_m \tau = 1$  on  $\mathbb{F}_\tau$ , and dividing by  $\varepsilon e^{T_{ji}}$  we obtain

$$0 = (L\varphi)_i + O(\varepsilon) \quad \text{on } \mathbb{R}, \text{ for all } i \in \mathbb{N}_m.$$

which implies Equation (D.1).  $\square$

*Remark D.2.* Note that the operator  $L$  depends on the coarse variables  $(c, T)$ , albeit we omit this dependence for notational simplicity.



We are now ready to define linear stability for a  $TW_m$ , which we adapt from [13]. Intuitively, we compare the firing set  $\mathbb{F}_\tau$  of a  $TW_m$  with the firing set  $\mathbb{F}_{\tau+\varphi}$  of a perturbed  $m$ -spike solution with  $\|\varphi\|_{C_{m,\eta}} \ll 1$ , for which  $\varphi$  satisfy (D.1) to leading order. If the sets  $\mathbb{F}_\tau$  and  $\mathbb{F}_{\tau+\varphi}$  are close around  $t = 0$  and remain close for all positive times, we deem the wave linearly stable. With reference to Figure 6(c), we observe that, when  $TW_m$  crosses the axis  $t = 0$ , each one of its firing functions  $\tau_i$  is perturbed by an amount  $\varphi_i(-cT_i)$ . Roughly speaking, a  $TW_m$  is linearly stable if  $\varphi_i(-cT_i)$  being small implies that  $\varphi_i(x)$  stays small for all  $x \in (-cT_i, \infty)$  and  $i \in \mathbb{N}_m$ . If a wave is linearly stable and all  $\varphi_i$  decay to 0 as  $x \rightarrow \infty$  we say that the wave is asymptotically linearly stable. More precisely:

**DEFINITION D.3** (Linear stability of  $TW_m$ ). *A  $TW_m$  with coarse variables  $(c, T)$  is linearly stable to perturbations  $\varphi$  if  $\varphi \in \ker L$ , and for each  $\varepsilon > 0$  there exists  $\delta = \delta(\varepsilon) > 0$ , such that if  $|\varphi_i(-cT_i)| < \delta$ , then  $|\varphi_i(x)| < \varepsilon$  for all  $(i, x) \in \mathbb{N}_m \times (-cT_i, \infty)$ .*

*A  $TW_m$  is asymptotically linearly stable to perturbations  $\varphi$  if is linearly stable to perturbations  $\varphi$  and  $|\varphi(x)|_\infty \rightarrow 0$  as  $x \rightarrow \infty$ .*

We have seen that a  $TW_m$  can be constructed by solving a nonlinear problem in the unknowns  $(c, T)$ . The following lemma, which is the central result of this section, establishes that linear stability of a  $TW_m$  with respect to exponential perturbations of the firing functions can also be determined by finding roots of a  $(c, T)$ -dependent, complex-valued function.

**LEMMA D.4** ( $TW_m$  stability). *Assume Hypothesis 3.1, let  $(c, T)$  be coarse variables of a  $TW_m$ , and let  $\mathbb{D}_{a,b} = \{z \in \mathbb{C} : a \leq \operatorname{Re} z \leq b\}$ . Further, let  $E$  be the complex-valued function*

$$(D.7) \quad E: \mathbb{D}_{-\eta,\eta} \rightarrow \mathbb{C}, \quad z \mapsto \det[D - M(z)],$$

where  $M \in \mathbb{C}^{m \times m}$ ,  $D = \operatorname{diag}(D_1, \dots, D_m) \in \mathbb{R}^{m \times m}$ , are the matrices with elements

$$M_{ij}(z) = e^{T_j i} \left[ 1_{j < i} + \int_{cT_{j_i}}^{\infty} e^{-(z+1/c)y} w(y) \psi_{ij}(y) dy \right], \quad D_i = \sum_{k \in \mathbb{N}_m} M_{ik}(0),$$

respectively, then:

1. *If  $\lambda$  is a root of  $E$ , then its complex conjugate  $\lambda^*$  is also a root of  $E$ , and there exists a nonzero  $\Phi \in \ker[D - M(\lambda)]$  such that  $\Phi e^{\lambda x}, \Phi^* e^{\lambda^* x} \in \ker L$ , where  $L$  is defined as in Lemma D.1.*
2.  *$E$  has a root at 0.  $TW_m$  is linearly stable (but not asymptotically linearly stable) to perturbations  $\varphi: x \mapsto \kappa v$ , where  $\kappa \in \mathbb{R} \setminus \{0\}$  and  $v = (1, \dots, 1) \in \mathbb{R}^m$ .*
3. *If  $\lambda$  is a root of  $E$  in  $\mathbb{D}_{-\eta,0} \setminus i\mathbb{R}$ , then  $TW_m$  is linearly asymptotically stable to perturbations  $\Phi e^{\lambda x} + \Phi^* e^{\lambda^* x}$ .*

*Proof. Part 1.* We observe that  $D$  has purely real entries, and a direct calculation shows  $M(z^*) = M^*(z)$ . If  $E(\lambda) = 0$ , then there exists  $\Phi \in \mathbb{C}^m \setminus \{0\}$  such that  $D\Phi = M(\lambda)\Phi$ , that is,  $\Phi \in \ker[D - M(\lambda)]$ . Taking the complex conjugate we obtain  $D\Phi^* = M^*(\lambda)\Phi^* = M(\lambda^*)\Phi^*$ , hence  $E(\lambda^*) = 0$ , therefore  $\lambda^*$  is also a root.

We now set  $\varphi = \Phi e^{\lambda x}$  which is in  $C_\eta(\mathbb{R}, \mathbb{C}^m)$  because  $\lambda \in \mathbb{D}_{-\eta,\eta}$ , and we obtain

$$(L\varphi)(x) = e^{\lambda x} [D - M(\lambda)]\Phi = 0 \quad x \in \mathbb{R}$$

because  $\Phi \in \ker[D - M(\lambda)]$ . The previous identity implies  $\Phi e^{\lambda x}, \Phi^* e^{\lambda^* x} \in \ker L$ .

*Part 2.* By definition of  $D$  and  $M$  we have  $[D - M(0)]v = 0$ , hence  $v$  is in the kernel of  $D - M(0)$  and  $E(0) = 0$ . We fix  $\kappa \in \mathbb{R} \setminus \{0\}$ , use part 1 with  $\lambda = 0$ ,  $\Phi = \kappa v$ , and deduce that the mapping  $\varphi: x \mapsto \kappa v$ , which is an element of  $C_\eta(\mathbb{R}, \mathbb{R}^m)$ , is in  $\ker L$ . Since  $\varphi_i(x) \equiv \kappa$ , for all  $i \in \mathbb{N}_m$ ,  $\text{TW}_m$  is linearly stable according to [Definition D.3](#). However,  $|\varphi(x)|_\infty \rightarrow \kappa \neq 0$  as  $x \rightarrow \infty$ , so  $\text{TW}_m$  is not asymptotically linearly stable.

*Part 3.* Let  $\lambda = \mu + i\omega$ . By main hypothesis  $\mu < 0$ . From part 1 we deduce that there exists  $\Phi \in \ker[D - M(\lambda)]$ , such that  $\varphi(x) = \Phi e^{\lambda x} + \Phi^* e^{\lambda^* x} \in \ker L$ . We note that  $|\Phi|_\infty$  can be fixed to an arbitrary nonzero constant, and we bound  $\varphi_i$  as follows [\(D.8\)](#)

$$|\varphi_i(x)| \leq 2|\Phi|_\infty e^{\mu x} \leq K|\Phi|_\infty, \quad K = 2 \max_{j \in \mathbb{N}_m} e^{-cT_j \mu}, \quad (i, x) \in \mathbb{N}_m \times [-cT_i, \infty).$$

We now fix  $\varepsilon > 0$ . The bound [\(D.8\)](#) and the choices  $\delta = \varepsilon$  and  $|\Phi|_\infty < \varepsilon/K$  imply that  $\text{TW}_m$  is linearly stable, according to [Definition D.3](#). Using again [\(D.8\)](#) we obtain

$$\lim_{x \rightarrow \infty} |\varphi(x)|_\infty \leq 2|\Phi|_\infty \lim_{x \rightarrow \infty} e^{\mu x} = 0$$

therefore  $\text{TW}_m$  is linearly asymptotically stable.  $\square$

[Lemma D.4](#) provides a link between exponential perturbations to the firing times of a  $\text{TW}_m$  and zeroes of the function  $E$  in the strip  $\mathbb{D}_{-\eta, \eta} \subset \mathbb{C}$ . The function  $E$  depends on  $(c, T)$  via the entries of the matrices  $D, M$ , and can be evaluated numerically at each point  $z \in \mathbb{D}_{-\eta, \eta}$ .

In PDEs, linear stability of a travelling wave is determined by the spectrum of a linear operator, which contains a 0 eigenvalue corresponding to a translational perturbation mode. Part 2 of [Lemma D.4](#) provides an analogous result for a  $\text{TW}_m$ , which is linearly stable, but not asymptotically linearly stable (therefore neutrally stable), to perturbations that shift the firing functions homogeneously. Part 3 of [Lemma D.4](#) suggests that a  $\text{TW}_m$  is stable if all nonzero roots of  $E$  have strictly negative real parts. Initial guesses for the roots can be obtained by plotting 0-level sets of the function  $E$ , for fixed  $(c, T)$ .

**Appendix E. Two-parameter continuation of bifurcations.** Grazing points are found generically as a secondary control parameter, say  $\gamma$ , is varied. It is possible to perform a 2-parameter continuation of the grazing point in the  $(\beta, \gamma)$ -plane by continuing in  $\gamma$  solutions the following problem:

*Problem E.1* (Grazing point computation). Find  $(c, T_1, \dots, T_m, T_G, \beta_G) \in \mathbb{R}_{>0} \times \mathbb{R}^{m+2}$  such that  $T_1 < \dots < T_m < T_G$  and

$$(E.1) \quad T_1 = 0,$$

$$(E.2) \quad \nu([cT_i]_-; c, T_1, \dots, T_m, \beta_G) = 1, \quad i \in \mathbb{N}_m,$$

$$(E.3) \quad \nu(cT_G; c, T_1, \dots, T_m, \beta_G) = 1,$$

$$(E.4) \quad \nu'(cT_G; c, T_1, \dots, T_m, \beta_G) = 0.$$

We note that we have exposed the dependence of  $\nu$  and  $\nu'$  on  $\beta$  in the previous problem. Unlike the numerical continuation presented in the main text, here  $\beta$  is a free parameter, which is determined also by Newton's method.

Similarly, we can trace loci of Hopf bifurcations in the  $(\gamma, \beta)$ -plane, by solving

*Problem E.2* (Computation of Hopf bifurcations). Find  $(c, T_1, \dots, T_m, \beta_{\text{HB}}, \omega_{\text{HB}}) \in$

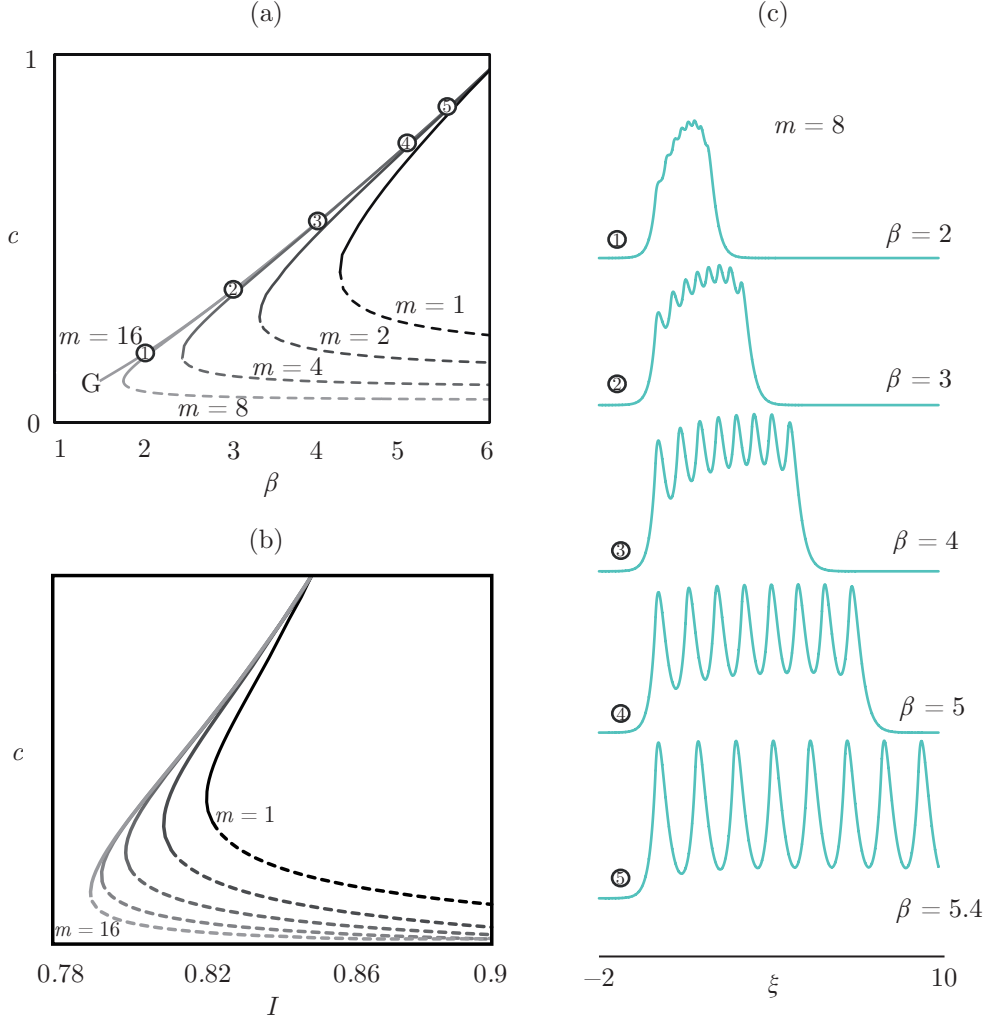


FIG. 13. Bifurcation diagram showing wave speed branches  $c$  for  $TW_m$  states with  $m = 1, 2, 4, 8, 16$ , with purely excitatory kernel,  $a_1 = 2$ ,  $b_1 = 5$ ,  $a_2 = 0$ . (a) External current is fixed at  $I = 0.82$  and solutions continued in  $\beta$ , here  $m = 1, 2, 4, 8$  branches switch stability at a fold, but for  $m = 16$  the branch terminates at a grazing point as seen in the lateral-inhibition case previously. (b) The synaptic processing rate is fixed at  $\beta = 4$  and the waves continued in  $I$ . Note that in both cases a greater  $m$  leads to larger speeds. (c) Synaptic profiles for  $TW_8$  solutions labelled (1–5) in (a). Smaller  $\beta$  values result in more localised profiles.

$\mathbb{R}_{>0} \times \mathbb{R}^{m+2}$  such that  $T_1 < \dots < T_m$  and

$$(E.5) \quad T_1 = 0,$$

$$(E.6) \quad \nu([cT_i]_-; c, T_1, \dots, T_m, \beta_{\text{HB}}) = 1, \quad i \in \mathbb{N}_m,$$

$$(E.7) \quad E(i\omega_{\text{HB}}; c, T_1, \dots, T_m, \beta_{\text{HB}}) = 0.$$

## REFERENCES

- [1] S.-i. AMARI, *Dynamics of pattern formation in lateral-inhibition type neural fields*, Biological Cybernetics, 27 (1977), pp. 77–87.
- [2] D. AVITABILE, *Numerical computation of coherent structures in spatially-extended systems*, May 2020, <https://doi.org/10.5281/zenodo.3821169>.
- [3] D. AVITABILE AND K. C. A. WEDGWOOD, *Macroscopic coherent structures in a stochastic neural network: from interface dynamics to coarse-grained bifurcation analysis*, Journal of Mathematical Biology, (2017), pp. 1–44.
- [4] J. BALADRON, D. FASOLI, O. FAUGERAS, AND J. TOUBOUL, *Mean-field description and propagation of chaos in networks of hodgkin-huxley and fitzhugh-nagumo neurons*, The Journal of Mathematical Neuroscience, 2 (2012), p. 10.
- [5] D. BARKLEY, *Simplifying the complexity of pipe flow*, Physical Review E, 84 (2011), p. 016309.
- [6] D. BARKLEY, *Pipe flow as an excitable medium*, Revista Cubana de Física, 29 (2012), pp. 1–27.
- [7] D. BARKLEY, *Theoretical perspective on the route to turbulence in a pipe*, Journal of Fluid Mechanics, 803 (2016).
- [8] D. BARKLEY, B. SONG, V. MUKUND, G. LEMOULT, M. AVILA, AND B. HOF, *The rise of fully turbulent flow*, Nature, 526 (2015), pp. 550–553.
- [9] C. BICK, M. GOODFELLOW, C. R. LAING, AND E. A. MARTENS, *Understanding the dynamics of biological and neural oscillator networks through mean-field reductions: a review*, Journal of Mathematical Neuroscience, 10 (2020), pp. 1–43.
- [10] P. C. BRESSLOFF, *Mean-field theory of globally integrate-and-fire neural oscillators with dynamic synapses*, Physical Review E, 60 (1999), p. 2160.
- [11] P. C. BRESSLOFF, *Synaptically generated wave propagation in excitable neural media*, Physical Review Letters, 82 (1999), pp. 2979–2982.
- [12] P. C. BRESSLOFF, *Traveling waves and pulses in a one-dimensional network of excitable integrate-and-fire neurons*, Journal of Mathematical Biology, 40 (2000), pp. 169–198.
- [13] P. C. BRESSLOFF, *Traveling waves and pulses in a one-dimensional network of excitable integrate-and-fire neurons*, Journal of Mathematical Biology, 40 (2000), pp. 169–198.
- [14] P. C. BRESSLOFF, *Waves in neural media*, Lecture Notes on Mathematical Modelling in the Life Sciences, Springer, New York, (2014).
- [15] P. C. BRESSLOFF AND S. COOMBES, *Dynamics of strongly-coupled spiking neurons.*, Neural Computation, 12 (2000), pp. 91–129.
- [16] A. N. BURKITT, *A review of the integrate-and-fire neuron model: I. Homogeneous synaptic input*, Biological Cybernetics, 95 (2006), pp. 1–19.
- [17] Á. BYRNE, D. AVITABILE, AND S. COOMBES, *Next-generation neural field model: the evolution of synchrony within patterns and waves*, Physical Review E, 99 (2019), p. 012313.
- [18] M. CAMPERI AND X.-J. WANG, *A model of visuospatial working memory in prefrontal cortex: recurrent network and cellular bistability*, Journal of Computational Neuroscience, 5 (1998), pp. 383–405.
- [19] A. COMPTE, N. BRUNEL, P. S. GOLDMAN-RAKIC, AND X.-J. WANG, *Synaptic mechanisms and network dynamics underlying spatial working memory in a cortical network model*, Cerebral Cortex, 10 (2000), pp. 910–923.
- [20] A. COMPTE, M. V. SANCHEZ-VIVES, D. A. MCCORMICK, AND X.-J. WANG, *Cellular and network mechanisms of slow oscillatory activity ( $\approx 1$  Hz) and wave propagations in a cortical network model*, Journal of Neurophysiology, 89 (2003), pp. 2707–2725.
- [21] S. COOMBES, P. BEIM GRABEN, AND R. POTTHAST, *Tutorial on Neural Field Theory*, in Neural Fields, Springer, Berlin, Heidelberg, Berlin, Heidelberg, 2014, pp. 1–43.
- [22] S. COOMBES, P. BEIM GRABEN, R. POTTHAST, AND J. WRIGHT, *Neural fields: Theory and Applications*, Springer, 2014.
- [23] S. COOMBES AND P. C. BRESSLOFF, *Saltatory waves in the spike-diffuse-spike model of active dendritic spines*, Physical Review Letters, 91 (2003), pp. 81–4.
- [24] S. COOMBES AND C. LAING, *Pulsating fronts in periodically modulated neural field models*, Physical Review E, 83 (2011), p. 011912.
- [25] S. COOMBES, H. SCHMIDT, AND D. AVITABILE, *Spots: breathing, drifting and scattering in a neural field model*, in Neural fields, Springer, Heidelberg, Berlin, Heidelberg, 2014, pp. 187–211.
- [26] A. DARBYSHIRE AND T. MULLIN, *Transition to turbulence in constant-mass-flux pipe flow*, Journal of Fluid Mechanics, 289 (1995), pp. 83–114.
- [27] F. DELARUE, J. INGLIS, S. RUBENTHALER, E. TANRÉ, ET AL., *Global solvability of a networked integrate-and-fire model of mckean-vaslov type*, The Annals of Applied Probability, 25 (2015), pp. 2096–2133.
- [28] M. DI BERNARDO, C. J. BUDD, A. R. CHAMPNEYS, P. KOWALCZYK, A. B. NORDMARK, G. O. TOST, AND P. T. PIHOINEN, *Bifurcations in Nonsmooth Dynamical Systems*, SIAM Re-

- view, 50 (2008), pp. 629–701.
- [29] J. R. DORMAND AND P. J. PRINCE, *A family of embedded Runge-Kutta formulae*, Journal of Computational and Applied Mathematics, 6 (1980), pp. 19–26.
- [30] B. ECKHARDT, H. FAISST, S. A., AND J. SCHUMACHER, *Turbulence transition in shear flows.*, in Advances in Turbulence IX: Proc. Ninth European Turbulence Conference, Barcelona, I. P. Castro, P. E. Hancock, and T. G. Thomas, eds., 2002, pp. 701–708.
- [31] B. ERMENTROUT, *Neural networks as spatio-temporal pattern-forming systems*, Reports on Progress in Physics, 61 (1998), p. 353.
- [32] B. ERMENTROUT, *The analysis of synaptically generated traveling waves*, Journal of Computational Neuroscience, 5 (1998), pp. 191–208.
- [33] B. ERMENTROUT, J. RUBIN, AND R. OŞAN, *Regular traveling waves in a one-dimensional network of theta neurons*, SIAM Journal on Applied Mathematics, 62 (2002), pp. 1197–1221.
- [34] G. B. ERMENTROUT, S. E. FOLIAS, AND Z. P. KILPATRICK, *Spatiotemporal pattern formation in neural fields with linear adaptation*, in Neural Fields, Springer, Berlin, Heidelberg, Berlin, Heidelberg, 2014, pp. 119–151.
- [35] G. B. ERMENTROUT AND N. KOPELL, *Parabolic bursting in an excitable system coupled with a slow oscillation*, SIAM Journal on Applied Mathematics, 46 (1986), pp. 233–253.
- [36] G. B. ERMENTROUT AND D. H. TERMAN, *Mathematical Foundations of Neuroscience*, vol. 35, Springer Science & Business Media, 2010.
- [37] J. M. ESNAOLA-ACEBES, A. ROXIN, D. AVITABILE, AND E. MONTBRIÓ, *Synchrony-induced modes of oscillation of a neural field model*, Physical Review E, 96 (2017), p. 052407.
- [38] H. FAISST AND B. ECKHARDT, *Traveling waves in pipe flow*, Physical Review Letters, 91 (2003), p. 224502.
- [39] S. E. FOLIAS AND P. C. BRESSLOFF, *Breathing pulses in an excitatory neural network*, SIAM Journal on Applied Dynamical Systems, 3 (2004), pp. 378–407.
- [40] S. E. FOLIAS AND G. B. ERMENTROUT, *Spatially Localized Synchronous Oscillations in Synaptically Coupled Neuronal Networks: Conductance-based Models and Discrete Maps*, SIAM Journal on Applied Dynamical Systems, 9 (2010), pp. 1019–1060.
- [41] W. GERSTNER, W. M. KISTLER, R. NAUD, AND L. PANINSKI, *Neuronal dynamics: from single neurons to networks and models of cognition*, Cambridge University Press, 2014.
- [42] W. GERSTNER, J. L. VAN HEMMEN, AND J. D. COWAN, *What matters in neuronal locking?*, dx.doi.org, 8 (2008), pp. 1653–1676.
- [43] J. F. GIBSON, J. HALCROW, AND P. CVITANOVIĆ, *Equilibrium and travelling-wave solutions of plane couette flow*, Journal of Fluid Mechanics, 638 (2009), pp. 243–266.
- [44] D. GOLOMB AND G. B. ERMENTROUT, *Continuous and lurching traveling pulses in neuronal networks with delay and spatially decaying connectivity*, Proceedings of the National Academy of Sciences, 96 (1999), pp. 13480–13485.
- [45] L. R. GONZÁLEZ-RAMÍREZ, O. J. AHMED, S. S. CASH, C. E. WAYNE, AND M. A. KRAMER, *A biologically constrained, mathematical model of cortical wave propagation preceding seizure termination*, PLoS Computational Biology, 11 (2015), pp. e1004065–34.
- [46] A. GRANADOS, L. ALSEDA, AND M. KRUPA, *The period adding and incrementing bifurcations: from rotation theory to applications*, SIAM Review, 59 (2017), pp. 225–292.
- [47] B. HOF, A. JUEL, AND T. MULLIN, *Scaling of the turbulence transition threshold in a pipe*, Physical Review Letters, 91 (2003), p. 244502.
- [48] E. HOPF, *A mathematical example displaying features of turbulence*, Communications on Pure and Applied Mathematics, 1 (1948), pp. 303–322.
- [49] X. HUANG, W. C. TROY, Q. YANG, H. MA, C. R. LAING, S. J. SCHIFF, AND J.-Y. WU, *Spiral waves in disinhibited mammalian neocortex*, J. Neurosci., 24 (2004), pp. 9897–9902.
- [50] J. INGLIS AND J. MACLAURIN, *A general framework for stochastic traveling waves and patterns, with application to neural field equations*, SIAM Journal on Applied Dynamical Systems, 15 (2016), pp. 195–234.
- [51] E. M. IZHIKEVICH, *Dynamical systems in neuroscience*, MIT press, 2007.
- [52] Z. P. KILPATRICK AND B. ERMENTROUT, *Wandering bumps in stochastic neural fields*, SIAM Journal on Applied Dynamical Systems, 12 (2013), pp. 61–94.
- [53] S. S. KIM, H. ROUAULT, S. DRUCKMANN, AND V. JAYARAMAN, *Ring attractor dynamics in the Drosophila central brain*, Science, 356 (2017), pp. 849–853.
- [54] J. J. KNIERIM AND K. ZHANG, *Attractor dynamics of spatially correlated neural activity in the limbic system*, Annual Review of Neuroscience, 35 (2012), pp. 267–285.
- [55] C. R. LAING, *Exact neural fields incorporating gap junctions*, SIAM Journal on Applied Dynamical Systems, 14 (2015), pp. 1899–1929.
- [56] C. R. LAING AND C. C. CHOW, *Stationary Bumps in Networks of Spiking Neurons*, Neural Computation, 13 (2001), pp. 1473–1494.

- [57] C. R. LAING AND O. OMEL'CHENKO, *Moving bumps in theta neuron networks*, Chaos: An Interdisciplinary Journal of Nonlinear Science, 30 (2020), p. 043117.
- [58] L. D. LANDAU, *On the problem of turbulence*, in Doklady Akademii Nauk USSR, vol. 44, 1944, p. 311.
- [59] L. LAPICQUE AND M. LAPICQUE, *Recherches quantitatives sur l'excitation électrique des nerfs traitée comme une polarisation*, Journal de Physiologie et de Pathologie Général, 9 (1907), pp. 620–635.
- [60] A. LITWIN-KUMAR AND B. DOIRON, *Slow dynamics and high variability in balanced cortical networks with clustered connections*, Nature Neuroscience, 15 (2012), pp. 1498–1505.
- [61] T. B. LUKE, E. BARRETO, AND P. SO, *Complete classification of the macroscopic behavior of a heterogeneous network of theta neurons*, Neural Computation, 25 (2013), pp. 3207–3234.
- [62] J. MACLAURIN AND P. ROBINSON, *Determination of effective brain connectivity from activity correlations*, Physical Review E, 99 (2019), p. 042404.
- [63] P. MANNEVILLE, *On the transition to turbulence of wall-bounded flows in general, and plane couette flow in particular*, European Journal of Mechanics-B/Fluids, 49 (2015), pp. 345–362.
- [64] A. MESEGUER AND L. N. TREFETHEN, *Linearized pipe flow to Reynolds number  $10^7$* , Journal of Computational Physics, 186 (2003), pp. 178–197.
- [65] R. E. MIROLLO AND S. H. STROGATZ, *Synchronization of pulse-coupled biological oscillators*, SIAM Journal on Applied Mathematics, 50 (2006), pp. 1645–1662.
- [66] E. MONTBRIÓ, D. PAZÓ, AND A. ROXIN, *Macroscopic description for networks of spiking neurons*, Physical Review X, 5 (2015), p. 021028.
- [67] R. OŞAN, R. CURTU, J. RUBIN, AND B. ERMENTROUT, *Multiple-spike waves in a one-dimensional integrate-and-fire neural network*, Journal of Mathematical Biology, 48 (2004), pp. 243–274.
- [68] R. OŞAN AND B. ERMENTROUT, *The evolution of synaptically generated waves in one- and two-dimensional domains*, Physica D: Nonlinear Phenomena, 163 (2002), pp. 217–235.
- [69] C. C. PRINGLE, Y. DUGUET, AND R. R. KERSWELL, *Highly symmetric travelling waves in pipe flow*, Philosophical Transactions of the Royal Society A: Mathematical, Physical and Engineering Sciences, 367 (2009), pp. 457–472.
- [70] J. RANKIN, D. AVITABILE, J. BALADRON, G. FAYE, AND D. J. LLOYD, *Continuation of localized coherent structures in nonlocal neural field equations*, SIAM Journal on Scientific Computing, 36 (2014), pp. B70–B93.
- [71] A. D. REDISH, A. N. ELGA, AND D. S. TOURETZKY, *A coupled attractor model of the rodent head direction system*, Network: Computation in Neural Systems, 7 (1996), pp. 671–685.
- [72] O. REYNOLDS, *An experimental investigation of the circumstances which determine whether the motion of water shall be direct or sinuous, and of the law of resistance in parallel channels*, Philosophical Transactions of the Royal Society of London, (1883), pp. 935–982.
- [73] K. A. RICHARDSON, S. J. SCHIFF, AND B. J. GLUCKMAN, *Control of Traveling Waves in the Mammalian Cortex*, Physical Review Letters, 94 (2005), p. 028103.
- [74] R. ROSENBAUM AND B. DOIRON, *Balanced Networks of Spiking Neurons with Spatially Dependent Recurrent Connections*, Physical Review X, 4 (2014), p. 021039.
- [75] D. RUELLE AND F. TAKENS, *On the nature of turbulence*, Les rencontres physiciens-mathématiciens de Strasbourg-RCP25, 12 (1971), pp. 1–44.
- [76] L. SACERDOTE AND M. T. GIRAUDO, *Stochastic integrate and fire models: a review on mathematical methods and their applications*, in Stochastic Biomathematical Models, Springer, 2013, pp. 99–148.
- [77] H. SALWEN, F. W. COTTON, AND C. E. GROSCH, *Linear stability of poiseuille flow in a circular pipe*, Journal of Fluid Mechanics, 98 (1980), pp. 273–284.
- [78] H. SCHMIDT AND D. AVITABILE, *Bumps and oscillons in networks of spiking neurons*, Chaos: An Interdisciplinary Journal of Nonlinear Science, 30 (2020), p. 033133.
- [79] A. SCHMIEGEL AND B. ECKHARDT, *Fractal stability border in plane couette flow*, Physical Review Letters, 79 (1997), p. 5250.
- [80] L. F. SHAMPINE AND M. W. REICHEL, *The MATLAB ODE suite*, SIAM Journal on Scientific Computing, 18 (1997), pp. 1–22.
- [81] M. L. STEYN-ROSS, D. A. STEYN-ROSS, J. W. SLEIGH, AND D. R. WHITING, *Theoretical predictions for spatial covariance of the electroencephalographic signal during the anesthetic-induced phase transition: increased correlation length and emergence of spatial self-organization*, Physical Review E, 68 (2003), p. 021902.
- [82] H. C. TUCKWELL, *Introduction to Theoretical Neurobiology. Volume 1: Linear Cable Theory and Dendritic Structure*, vol. 8, Cambridge University Press, 1988.
- [83] D. TURNER-EVANS, S. WEGENER, H. ROUAULT, R. FRANCONVILLE, T. WOLFF, J. D. SEELIG,

- S. DRUCKMANN, AND V. JAYARAMAN, *Angular velocity integration in a fly heading circuit*, eLife, 6 (2017), p. e23496.
- [84] C. W. VAN DOORNE AND J. WESTERWEEL, *The flow structure of a puff*, Philosophical Transactions of the Royal Society A: Mathematical, Physical and Engineering Sciences, 367 (2009), pp. 489–507.
- [85] C. VAN VREESWIJK, *Partial synchronization in populations of pulse-coupled oscillators*, Physical Review E, 54 (1996), pp. 5522–5537.
- [86] C. VAN VREESWIJK, L. F. ABBOTT, AND G. B. ERMENTROUT, *When inhibition not excitation synchronizes neural firing*, Journal of Computational Neuroscience, 1 (1994), pp. 313–321.
- [87] C. V. VREESWIJK AND H. SOMPOLINSKY, *Chaotic Balanced State in a Model of Cortical Circuits*, Neural Computation, 10 (1998), pp. 1321–1371.
- [88] H. WEDIN AND R. R. KERSWELL, *Exact coherent structures in pipe flow: Travelling wave solutions*, Journal of Fluid Mechanics, 508 (2004), pp. 333–371.
- [89] H. R. WILSON AND J. D. COWAN, *A mathematical theory of the functional dynamics of cortical and thalamic nervous tissue*, Kybernetik, 13 (1973), pp. 55–80.
- [90] K. WIMMER, D. Q. NYKAMP, C. CONSTANTINIDIS, AND A. COMPTE, *Bump attractor dynamics in prefrontal cortex explains behavioral precision in spatial working memory*, Nature Neuroscience, 17 (2014), pp. 431–439.
- [91] M. WOLFRUM, O. E. OMEL'CHENKO, AND J. SIEBER, *Regular and irregular patterns of self-localized excitation in arrays of coupled phase oscillators*, Chaos: An Interdisciplinary Journal of Nonlinear Science, 25 (2015), pp. 053113–8.
- [92] K. ZHANG, *Representation of spatial orientation by the intrinsic dynamics of the head-direction cell ensemble: a theory*, Journal of Neuroscience, 16 (1996), pp. 2112–2126.